UNIVERSITY OF HELSINKI REPORT SERIES IN PHYSICS

HU-P-D99

Heavy Ion Recoil Spectroscopy of Surface Layers

Timo Sajavaara

Accelerator Laboratory
Department of Physical Sciences
Faculty of Science
University of Helsinki
Helsinki, Finland

ACADEMIC DISSERTATION

To be presented, with the permission of the Faculty of Science of the University of Helsinki, for public criticism in the Small Auditorium (E204) of Physicum, on October 5th, 2002 at 12 o'clock noon.

HELSINKI 2002

ISBN 951-45-8952-1 (printed version)
ISSN 0356-0961
Helsinki 2002
Yliopistopaino

ISBN 952-10-0560-2 (PDF version)
http://ethesis.helsinki.fi/
Helsinki 2002
Helsingin yliopiston verkkojulkaisut

T. Sajavaara: **Heavy Ion Recoil Spectroscopy of Surface Layers**, University of Helsinki, 2002, 65 p.+appendices, University of Helsinki Report Series in Physics, HU-P-D99, ISSN 0356-0961, ISBN 951-45-8952-1 (printed version), ISBN 952-10-0560-2 (PDF version)

Classification (INSPEC): A8280, A6855
Keywords: Elastic recoil detection, detection efficiency, multiple scattering, surface roughness, atomic layer deposition

ABSTRACT

Determination of atomic concentration distributions in thin films is a key problem in materials science. The optimisation process of the thin film growth parameters in particular requires detailed information about the elemental concentrations of the main constituents and undesired impurities. So far, the characterisation methods capable of a depth-sensitive analysis of all elements have remained limited.

In the research for this thesis, the concentration distributions of elements in surface layers were studied using heavy ion elastic recoil detection analysis (HI-ERDA). The analysis was expanded to include hydrogen and the heaviest elements. The energy-dependent detection efficiency of the time-of-flight energy telescope was determined for the lightest elements.

The reliability of the concentration distributions obtained was seen to be strongly affected by the multiple scatterings of the ions and surface roughness of the sample. Both of them were studied by comparing Monte Carlo simulation results with the experimental ones. The surface topographies used in the simulations were determined with a scanning probe microscope.

The analysis procedures developed were applied to characterise novel materials such as atomic layer deposited thin films used in future integrated circuit designs and pulsed vacuum arc deposited thin films, which are candidates for fusion reactor wall materials.

Contents

1 INTRODUCTION 6

2 PURPOSE AND STRUCTURE OF THIS STUDY 8

3 PRINCIPLES OF HEAVY ION SPECTROSCOPY 10

3.1 Ion energy loss 10

3.2 Scattering kinematics and scattering cross section 12

4 PROGRESS IN TIME-OF-FLIGHT ELASTIC RECOIL DETECTION MEASUREMENTS 15

4.1 Setup in the Accelerator Laboratory 16

4.2 Detection efficiency 19

4.2.1 Electron emission and multiplication 19

4.2.2 Discriminator threshold 21

4.3 Hydrogen analysis 23

4.4 Forward scattering analysis 24

5 COMPLEMENTARY MEASUREMENTS 26

5.1 Nuclear reaction analysis and Rutherford backscattering spectrometry 26

5.2 Other thin film characterisation methods 28

5.2.1 Secondary ion mass spectrometry 28

5.2.2 Scanning electron microscopy 28

5.2.3 X-ray photoelectron spectroscopy 29

5.2.4 Scanning probe microscopy 30

6 PROGRESS IN THE ANALYSIS PROCEDURE AND RESULTS OBTAINED 31

6.1 Beam quality and measurement geometry effects 31

6.2 Selection of ions 33

6.3 Concentration determination 35

6.3.1 Energy spectrum 35

6.3.2 Stopping power independent concentration determination 35

6.3.3 Calculation of concentration distributions 37
6.3.4 TOF-ERDA performance 38
6.4 Multiple and plural scattering 38
6.5 Surface roughness 42
6.6 Ion beam induced modification 45
6.6.1 Sputtering and elemental losses 45
6.6.2 Destruction of the crystalline structure 47
6.7 Summary of TOF-ERDA results 49

7 CONCLUSIONS AND CONSIDERATIONS FOR FUTURE RESEARCH 52

ACKNOWLEDGEMENTS 53

REFERENCES 54

1 INTRODUCTION

The need for better characterisation methods is a driving force in the ion beam analysis community. The requirements differ. For one the first atomic layers at the surface are the focus of interest, and for another what is fascinating occurs at the depth of tens of micrometres. In this thesis, surface layers denote sample structures which can be probed with ion beam analysis methods. Today miniaturisation in semiconductor industry has directed the research towards smaller dimensions and structures. The central part of this research is concerned with thin films, and the demand for high performance characterisation methods is growing.

The functionality of a device or thin film in a device is an outcome of their properties. For a deeper understanding of the behaviour of a transistor and an optical device, the characteristic properties of all the components, such as conductors, insulators, electrical junctions, and semiconductors, have to be known. Since thin films are a major part of the research in semiconductor industry, the development and usability of the characterisation methods for them are of great importance.

Growth methods used for thin film deposition depend on the application and scale of production. Some of the deposition methods are scalable from research size deposition up to mass production like magnetron sputtering. Depending on the properties required of the layers to be grown, a suitable method is chosen. From microelectronic industry's viewpoint, a very attractive deposition technique is atomic layer deposition (ALD) [1], a Finnish invention which is a chemical vapour deposition (CVD) method with excellent characteristics such as good step coverage, low growth temperatures, and accurate film thickness control. ALD-grown high-*k* oxides can be the solution that takes us to the terahertz era in processor performance when SiO_2 is replaced by other gate oxide materials [2].

Because of the great variety of thin film types, compositions, and applications, there is a large number of vital properties to be studied. These properties include, for example, refraction index in optical coatings, permittivity and resistivity for insulating films, emission colour and brightness for electroluminescent films, and wear resistance for hard coatings. Moreover there are qualities like film composition and surface structure which are always significant and therefore needed in a complete interpretation. Acquaintance with these characteristics is the key to the understanding other properties.

For composition determination, energetic ion beams have been used since the early twentieth century and Ernst Rutherford's days. Initially the methods used were qualitative and not depth sensitive. After the Second World War the wide availability of single-ended Van de Graaff accelerators gave rise to ion beam analysis. Through the development of surface barrier energy detectors made of high purity silicon and data collection facilities these methods became to be widely used. The driving force was, like it is today, the rapid development of microelectronics. Rutherford Backscattering Spectrometry (RBS) provided a tool for quantitative depth profiling of elements. Today ion beam analysis methods like RBS, elastic recoil detection analysis (ERDA), and nuclear reac-

tion analysis (NRA) are applied to solve a variety of problems, *e.g.* film constituents, diffusion behaviour, and impurity atom location in a lattice.

Forward scattered energetic recoil atoms were used in depth profiling for the first time in 1976, when L'Ecuyer *et al*. published the results of a study in which they had detected recoils using incident 25–40 MeV ^{35}Cl ions [3]. After a quarter of a century, the ERDA methods can now be divided coarsely into two groups: incident light ion ERDA utilises low voltage single ended accelerators, and incident heavy ion ERDA (HI-ERDA) mainly uses large tandem accelerators built originally for nuclear physics research. The latter are usually equipped with element or mass sensitive detectors. The suitability of HI-ERDA for the depth profiling of light atoms has been generally acknowledged, but the utilisation of forward scattered incident ions broadens the analysis to the heaviest atoms.

In HI-ERDA, some factors, such as multiple scattering and ion beam induced damage, have to be taken into consideration. These two are not strong effects when light projectiles like He and Li are used. In addition to these two, also the glancing angles of in-going and out-coming particles make the surface topography related effects important in the interpretation of the results. By including surface topography information into ion beam analysis, a reliable elemental characterisation of the surface layers can be obtained.

In the 1980s, surface characterisation moved from larger structures to a range of individual atoms after Binnig *et al*. made the first scanning tunnelling microscope (STM) in 1982 [4,5]. It was the first time atoms, lattice defects, and atomic planes could be seen in structures. Together with atomic force microscopy (AFM) [6], this and related techniques have revolutionised surface research. A common name for these methods is scanning probe microscopy (SPM). The lateral resolution of AFM and STM is better than that of the other surface characterisation methods.

Quantitative depth profiling of all the sample atoms in one measurement is now in the focus of inclusive research. It can be achieved by means of HI-ERDA. This technique has been found to be especially useful in the characterisation of silicon dioxide replacing ALD-grown dielectric films. The depth profiling applicability of the method is much larger and extends, for example in this thesis, from the first wall materials of the fusion reactor to future solar cell materials.

2 PURPOSE AND STRUCTURE OF THIS STUDY

The purpose of the present study was to improve the versatility and credibility of ERDA when incident high energy heavy ions and time-of-flight-energy (TOF-E) telescope are employed. The usability of heavy ions in the analysis of thin films and different materials were dealt with. The method was applied to the characterisation of a number of novel materials.

The following papers and the present introductory section constitute this thesis. In the introductory section the papers are referred to by Roman numbers. In papers I–III the measurement system and heavy ion ERDA characteristics are dealt with. Paper IV represents a study in which TOF-ERDA was applied to analyse challenging ALD deposited thin films with light and very heavy constituents. Complementary characterisation methods were used in papers V and VI. Paper VII represents a migration study performed with TOF-ERDA.

Paper I: Y. Zhang, H.J. Whitlow, T. Winzell, I.F. Bubb, **T. Sajavaara**, K. Arstila, and J. Keinonen, *Detection Efficiency of time-of-flight energy elastic recoil detection analysis systems*, Nuclear Instruments and Methods in Physics Research B, **149** (1999) 477.

> Energy dependent detection efficiencies for the TOF-E telescopes in Uppsala and Helsinki were determined and compared for different elements. Different factors governing the detection efficiency are discussed in detail and empirical elemental fitting functions for energy dependent detection efficiencies are presented.

Paper II: K. Arstila, **T. Sajavaara**, and J. Keinonen, *Monte Carlo simulation of multiple scattering effects in elastic recoil detection*, Nuclear Instruments and Methods in Physics Research B, **174** (2001) 163.

> The multiple and plural scattering and their importance in HI-ERDA are dealt with and a high performance Monte Carlo (MC) simulation program for ERD energy spectra is developed.

Paper III: T. Sajavaara, K. Arstila, A. Laakso, and J. Keinonen, *Effects of surface roughness on results in elastic recoil detection measurements*, Nuclear Instruments and Methods in Physics Research B, **161–163** (2000) 235.

> Surface roughness effects are dealt with for thin film layers on a rough substrate. Experimental ERD results are compared with those obtained in MC simulations using a topography measured with AFM.

Paper IV: P. Alen, M. Juppo, M. Ritala, M. Leskelä, **T. Sajavaara**, and J. Keinonen, *Tert-butylamine and allylamine as reductive nitrogen sources in atomic layer deposition of TaN thin films*, Journal of Materials Research, **17** (2002) 107.

> TaN, a candidate for diffusion barrier material in electrodes of microelectronics, is characterised by means of TOF-ERDA, energy dispersive X-ray spectroscopy and X-ray diffraction. In TOF-ERDA, the forward scattered projectiles were utilised in Ta depth profiling.

Paper V: M. Kemell, M. Ritala, H. Saloniemi, M. Leskelä, **T. Sajavaara**, and E. Rauhala, *One-step electrodeposition of* $Cu_{2-x}Se$ *and* $CuInSe_2$ *thin films by the induced co-deposition mechanism*, Journal of the Electrochemical Society, **147** (2000) 1080.

Thin films grown by a one-step electrodeposition method are studied by means of scanning electron microscopy, energy dispersive X-ray spectroscopy, X-ray diffraction, and ion beam analysis using TOF-ERDA and RBS.

Paper VI: E. Vainonen-Ahlgren, T. Ahlgren, J. Likonen, S. Lehto, **T. Sajavaara**, W. Rydman, J. Keinonen, and C.H. Wu, *Deuterium diffusion in silicon-doped diamond-like carbon films*, Physical Review B, **63** (2001) 045406.

Diffusion of deuterium in diamond-like carbon films with different silicon contents (0–33 at.%) is studied. Secondary-ion-mass spectrometry (SIMS) and TOF-ERDA are used for the depth profile determination of elements.

Paper VII: T. Sajavaara, R. Lappalainen, K. Arstila, W.-M. Li, M. Ritala, M. Leskelä, and E. Soininen, *Modification of ALE-grown SrS thin films by ion implantation of Cu and codopants*, Nuclear Instruments and Methods in Physics Research B, **148** (1999) 715.

ALD-grown SrS thin films were implanted with Cu ions and then coimplanted with Cl and O ions. Diffusion behaviour of these ions and photoluminescence characteristics are studied for annealed films.

The above papers are the product of a group effort. My contribution to the related experimental work was concerned with detection efficiency measurements in the Accelerator Laboratory of the University of Helsinki [I], sample preparation and ion beam analysis [II], AFM and ion beam analysis [III], and TOF-ERD analysis [IV–VII]. In addition, the ERD analysis techniques developed for this thesis have been utilised for the data in the papers [7–35] for which I did the TOF-ERD analysis and the AFM, and scanning electron microscopy measurements. The MC simulation program used in papers II and III was written by Dr. Kai Arstila. I was the responsible author in papers III and VII, had a major contribution in writing papers I and II, and participated in writing papers IV-VI.

Chapter 3 will introduce the principles of the physical processes involved in heavy ion spectroscopy. The progress in the TOF-ERDA measurements in the Accelerator Laboratory will be dealt with in chapter 4 and additional results to paper I are presented. The progress in the analysis procedure done for this thesis and some application examples will be taken up in chapter 4. The measurements complementary to TOF-ERDA used in this thesis will be discussed in chapter 5. In chapter 6 main factors affecting heavy ion spectroscopy will be dealt with in a view of the papers II and III, the progress in the analysis procedure, and the main results of TOF-ERD analyses of various thin films are presented. Chapter 7 will present conclusions and some considerations for future research in this area.

3 PRINCIPLES OF HEAVY ION SPECTROSCOPY

Every depth sensitive analysis method which utilises energetic ion beams, is based on the energy loss of ions traversing in a material. Therefore it is necessary to be acquainted with ion energy loss phenomena. The yield and kinematics in ion beam methods also depend on the scattering process which will be described with classical equations below.

3.1 Ion energy loss

An ion which penetrates material loses its energy when interacting with sample atoms. The interactions are usually divided into two separate processes, namely energy loss in elastic collisions with sample atom nuclei (nuclear stopping power) and inelastic collisions with electrons (electronic stopping power). In ion beam analysis, if the density of a target material is known, an energy loss in units keV/nm can be used. The quantity is widely called stopping power of the target material for a penetrating ion, despite the fact that it really is a resistive force instead of power. If the density of a material is not known, the density independent stopping cross-sections in unit eV/(10^{15}atoms/cm^2) are used in the analysis.

As can be seen from Fig. 1, nuclear energy loss dominates in the low velocity (energy) region but electronic energy loss is much larger in high velocities. The parameterisation used for the calculation of the nuclear stopping power is based on the universal inter-atomic potential by Ziegler *et al*. [36]. When the velocity of a moving ion is increased, it loses its electrons and becomes more and more positively charged. At high velocities the ions become totally stripped from electrons. In the basis of the theory by Brandt and Kitagawa (BK theory) [37], Ziegler, Biersack and Littmark created a semiempirical parameterisation (ZBL parameterisation) for the calculation of the electronic stopping powers for every ion in every material [36]. The functional shape of this most widely used parameterisation is based on the extensively studied experimental stopping powers reported for H.

For helium ions the stopping power is the equivalent hydrogen stopping at the same velocity multiplied by the effective charge of He ions at the velocity in question. The stopping powers are always scaled to velocities, not to energies. The effective charge is calculated with a parameterisation, which is obtained by fitting to a constructed function all the available experimental H and He stopping power data [36, 39]. For heavy ions the stopping power curve can be divided into three different velocity regions [36]: (a) very low velocities, where the stopping powers are proportional to the ion's velocity, (b) high velocities, where the proton stopping powers can be scaled to obtain heavy ion stopping powers, and (c) a medium velocity region between the two regions. The medium velocity region requires the most complex theory. The projectile energy range used in the ion beam analysis utilising heavy ions is in the complex region (c). Most of the detected light atoms lose their energy in the high velocity region (b). In Fig. 1 the nuclear and electronic stopping powers of

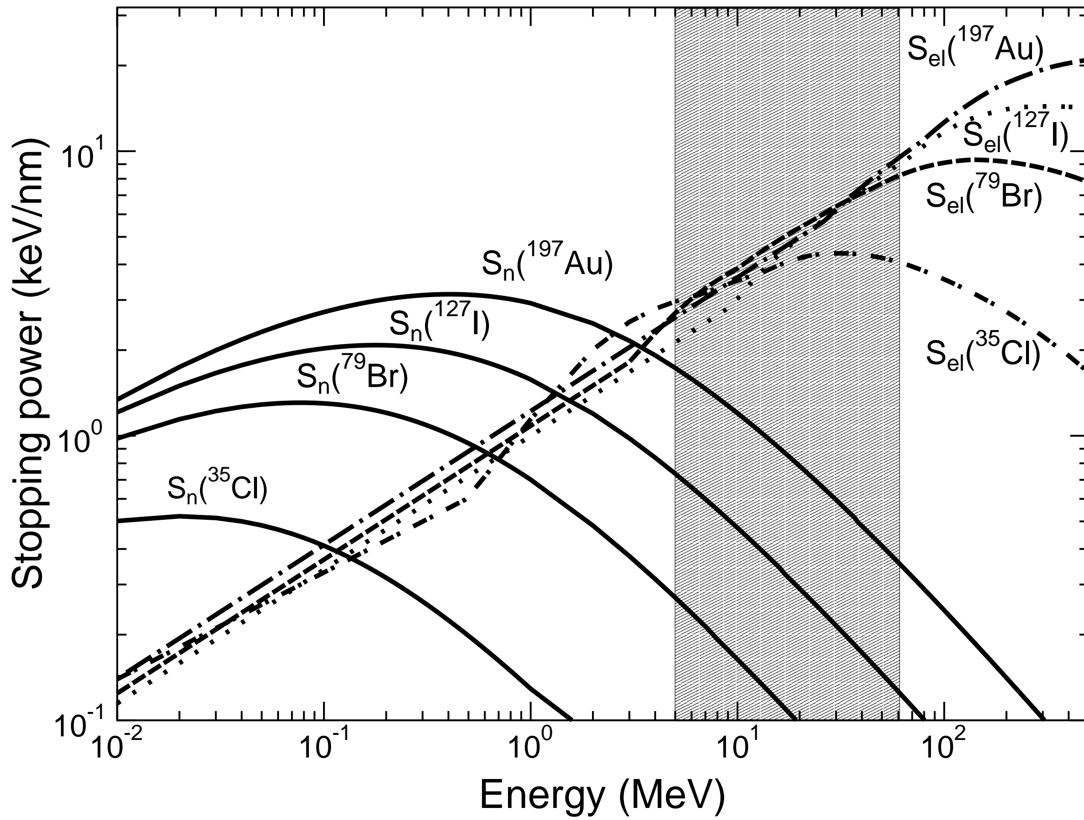

Figure 1: Nuclear (S_n) and electronic (S_{el}) stopping powers of silicon for the ^{35}Cl, ^{79}Br, ^{127}I, and ^{197}Au ions calculated using the ZBL parameterisation [36, 38]. The energy region relevant in the TOF-ERD analysis in the Accelerator Laboratory is shadowed.

silicon are plotted for ^{35}Cl, ^{79}Br, ^{127}I, and ^{197}Au ions in the energy range of 0.01–500 MeV in the framework of the ZBL-parameterisation. These ions have been utilised in this thesis, and they are the most used ones in HI-ERDA in the literature.

As there is no first-principles theory to calculate the stopping powers, more experimental stopping power data are required for different ion-material combinations. The data can then be used in the fittings to the semiempirical models to increase the accuracy of the stopping powers reproduced by the ZBL model. The inaccuracy of the ZBL parameterisation for heavy ions can be as high as 20% [40]. The reason for the uncertainties are the incorrect shapes of the functions used in the fittings and the large scattering of the experimental data.

In the Accelerator Laboratory, techniques have been developed to measure the electronic stopping powers by means of the inverted Doppler shift attenuation method (IDSA). The velocity dependency of the stopping powers has been obtained for Mg [41, 42], Si [40, 43], and P ions [43]. To fulfill the growing need for heavy ion stopping cross-sections in various materials, a novel method has recently been introduced by Zhang *et al.*, where a TOF-E telescope was utilised to measure the stopping powers of self-supporting films for a variety of ions [44, 45] and over a wide energy range. The same method was simultaneously independently used by Trzaska *et al.* [46, 47].

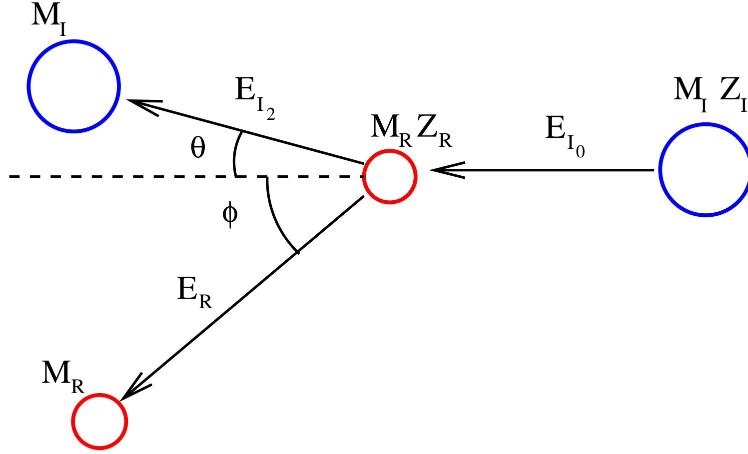

Figure 2: Schematic picture of a heavy ion elastic scattering. The subscripts I and R denote the incident and recoil ions, respectively.

Due to the statistical fluctuations in the number of collision processes, energy spread or energy straggling is also present during the slowing down. On the basis of a fitting function by Chu [48], Yang *et al*. performed a fit to the experimental straggling data for H, He, and heavy ions [49]. The deduced parameterisation applies only to the energy loss and does not include the angular spread.

The surface layers in ion beam analysis mostly contain more than one element. For calculating stopping power of the samples of compound materials an additivity rule by Bragg and Kleeman is applied [50]. According to this *Bragg′s rule*, the stopping cross-sections of elements multiplied by their atomic concentration percentage in a compound are added to get the stopping cross-section of the compound. This simplified approximation does not take into account the realistic electron densities of the compound matter.

Despite the need for accurate stopping power data of compounds, not many publications are found on the topic in the literature. One reason is the fact that the preparation of representative self-supporting thin films out of compounds is difficult in most cases and the conventional transmission method is difficult to use for the stopping power measurements. In this method the ion energy loss in a self-supporting film is measured, and area and mass of the film are determined and the stopping cross-section is deduced. The IDSA measurements can be done well for bulk samples, and the stopping powers can be obtained, as is indicated by an example for Si in ceramics [51].

3.2 Scattering kinematics and scattering cross section

In ERDA the scattering of an energetic ion with a sample atom is regarded as a classical two-body collision where the only force present is the Coulomb repulsion between two bare nuclei as illustrated in Fig. 2. In an elastic collision the energy and momentum are conserved and the

final energy of both the projectile and the target atom can be calculated exactly. In the laboratory coordinates the final energy of a target atom with the mass M_R hit by a projectile with the mass M_I and energy E_I is obtained from the following equation:

$$E_R = \left(\frac{4 M_I M_R \cos^2\phi}{(M_I + M_R)^2} \right) E_{I_0} \equiv \Lambda E_{I_0}, \tag{1}$$

where ϕ is the recoil angle and Λ is called the kinematic factor. Similarly, a projectile scattered to the angle θ has an energy of

$$E_{I_2} = E_{I_0} - E_R = \left(\frac{\sqrt{M_R^2 - M_I^2 \sin^2\theta} \pm M_I \cos\theta}{M_I + M_R} \right)^2 E_{I_0} \equiv K_1 E_{I_0}. \tag{2}$$

If $M_I > M_R$, the equation has two solutions as illustrated in Fig. 3a, where the final energies of both the ^{140}Ce recoil and the ^{197}Au projectile are drawn as a function of the scattering angle. The two solutions in the Eq. (2) denote that the incident ^{197}Au ions may scatter to the angle θ with two different energies. When $M_I > M_R$, the maximum scattering angle θ_{max} is determined by the positive solution of the square root in Eq. (2) and

$$\theta_{max} = \arcsin \frac{M_R}{M_I}. \tag{3}$$

If the heaviest element in the sample is ^{140}Ce, the maximum angle for the direct scattering of a ^{197}Au projectile is 45.3°. If $M_I \leq M_R$ the numerator in Eq. (2) is a sum. This is illustrated in Fig. 3b, where the final energies of the ^{127}I projectile and ^{140}Ce recoil atom are drawn as a function of the scattering angle. The elastic scattering cross-sections or scattering probabilities can be deduced by using the Coulomb potential

$$V(r) = \frac{1}{4\pi\varepsilon_0} \frac{Z_I Z_R e^2}{r}, \tag{4}$$

where e is the unit of the electrical charge, ε_0 the permittivity for a vacuum, and Z_1 and Z_R are atomic numbers of the projectile and the recoil atom, respectively. If the scattering occurs within the radius of K-shell electrons, it can be treated as a pure Coulomb scattering. This scattering is also often called the Rutherford scattering contrary to scatterings between two nuclei shadowed by electrons in the low energy region or two nuclei approaching so close to each other in high energy collisions that the nuclear force affects the scattering cross-section. In the laboratory coordinates the differential cross-section for recoil atoms is

$$\frac{d\sigma_R}{d\Omega} = \left(\frac{Z_I Z_R e^2}{8\pi\varepsilon_0 E_0} \right)^2 \frac{(1 + M_I/M_R)^2}{\cos^3\phi}. \tag{5}$$

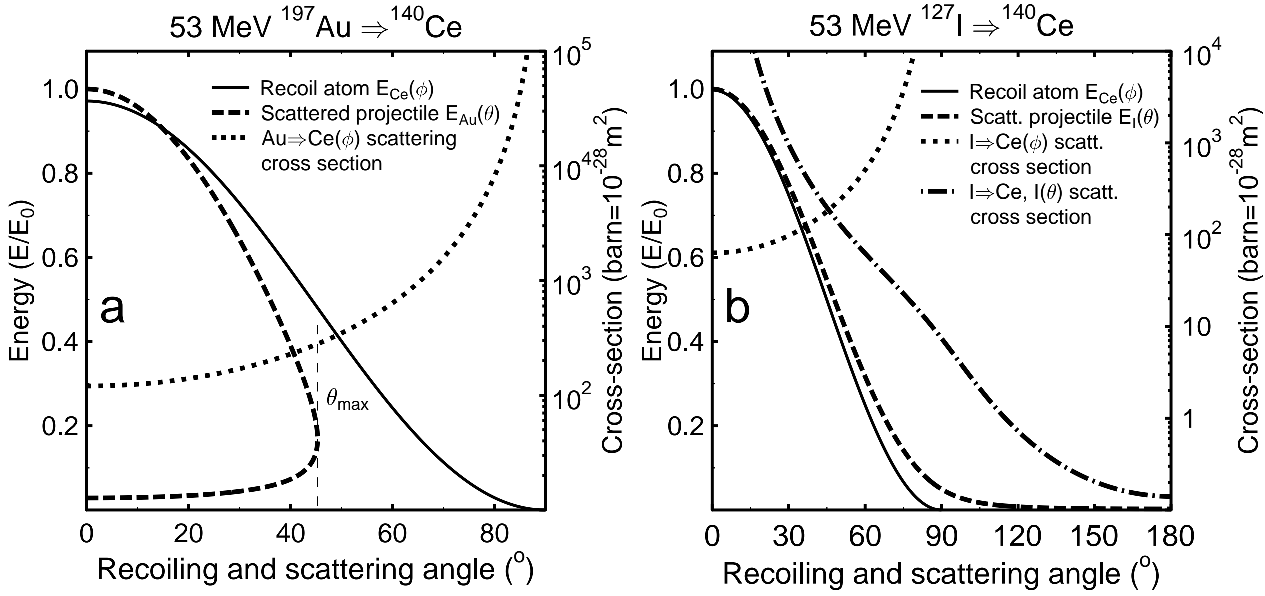

Figure 3: Elastic scattering energies and cross-sections of recoil atoms and scattered projectiles as a function of the scattering angle. Cross-sections are calculated for 53 MeV ^{197}Au→^{140}Ce (a) and 53 MeV ^{127}I→^{140}Ce (b) collisions. These ions and energies are typical in HI-ERDA. The typical total scattering angle (ϕ for recoils and θ for incident ions) varies between 35° and 45°. Notice the different scales for the cross-section and scattering angles in (a) and (b).

Differential scattering cross-sections for Ce recoils are shown in Fig. 3. For scattered projectiles the differential cross section is given by the following equation:

$$\frac{d\sigma_I}{d\Omega} = \left(\frac{Z_I Z_R e^2}{8\pi\varepsilon_0 E_0}\right)^2 \frac{\left(\sqrt{(M_R^2 - M_I^2 \sin^2\theta} \pm M_R \cos\theta\right)^2}{M_R \sin^4\theta \sqrt{M_R^2 - M_I^2 \sin^2\theta}}. \tag{6}$$

Again, if $M_I > M_R$ the Eq. (6) has two solutions and the incident ion can be detected at the same angle θ with two different energies and scattering cross-sections. The scattering probability of incident ions increases when scattering angle decreases. The behaviour is an opposite to that of the recoil scattering. These two scattering cross-sections determined by Eqs. (5) and (6) are illustrated in Fig. 3b.

4 PROGRESS IN TIME-OF-FLIGHT ELASTIC RECOIL DETECTION MEASUREMENTS

The idea of ERDA is to detect forward scattered sample atoms and use the stopping power, scattering cross-section, and kinematics to determine the concentration distributions of different elements. The the first measurements were performed using transmission geometry [3]. More attention attracted a method where the projectiles went in and the recoils came out from the same side of the sample (see Fig. 4) and the recoil energy spectrum was measured [52, 53]. With this setup it was also possible to analyse other samples than self-supporting films.

In the setup used in the research for this thesis, the original depth d of the recoil atom in the sample was determined by using the knowledge of the recoil final energy E_R, incident ion energy E_{I_0}, the stopping powers of the recoil and the incident ions in the sample along the paths $d/\sin(\beta)$ and $d/\sin(\alpha)$, respectively, and the kinematic factor Λ. These terms are illustrated in Fig. 4. The number of the detected recoils Y in a detector solid angle $d\Omega$ during an irradiation of a sample thickness dx by N incident ions is given by the equation

$$Y = N d\Omega dx \frac{d\sigma}{d\Omega}, \tag{7}$$

where $d\sigma/d\Omega$ is the differential recoiling cross-section (m^{-28}at.$^{-1}$sr^{-1}) and dx the ion path length in a sample (at.cm^{-2}).

Although the measurements are usually performed in a symmetrical geometry ($\alpha = \beta$), the depth resolution can be made better and scattering yields higher by tilting the sample (smaller α and larger β) without changing the total scattering angle θ. This has the disadvantage that the surface roughness effects become stronger and, for a constant beam intensity per sample area, the ion beam induced damage is enhanced.

In the first ERDA measurements reported in the literature [3, 53], a surface barrier energy detector was used for particle detection. Polymer or metallic films were used in front of the detector both to protect it from scattered incident ions and to separate different recoil elements. The separation is based on different stopping powers and kinematic factors for different atoms. With a careful selection of the detector angle and absorber thickness, a separation of 3–4 light elements or isotopes in a heavy atom matrix was possible.

Due to the limited applicability of the conventional method, new ERDA setups with a more efficient separation of elements were designed. These include solid state ΔE-E detectors [54, 55] and gas ionisation ΔE-E detectors [56–60] with element separation and position sensitivity, magnetic spectrometers with charge-mass sensitive separation [61], and TOF-E detectors with mass sensitive separation [62, 63].

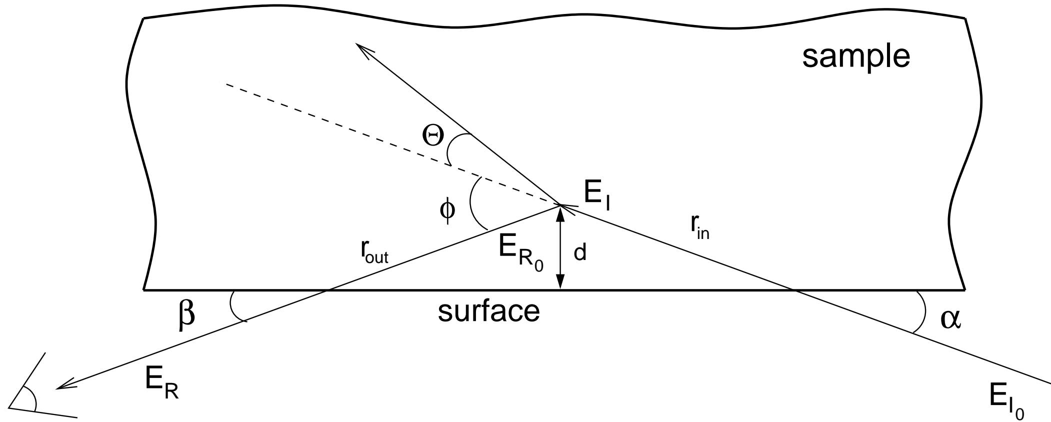

Figure 4: Scattering geometry of an ERDA experiment.

4.1 Setup in the Accelerator Laboratory

There are a number of different measurement setups for TOF-ERDA. For instance, the time of flight can be determined by means of two identical timing gates [63–66] or an energy detector can be used to obtain the timing signal [62, 67]. The energy spectra are usually deduced from TOF-spectra, because TOF-detector has a linear calibration for all ions. The calibration is also independent of the irradiation damage, in contrary to charged particle detectors. The energy resolution of the TOF-detector for heavy ions is better and for light ions like C, N, and O of the same order than that of charged particle detector. A solitary high energy resolution TOF-detector can also be used in forward or backscattering geometry [68].

The TOF-ERDA setup used in the research for this thesis consists of two timing gates constructed according to those by Busch *et al.* [69] and an ion implanted energy detector. The measurement system is described in more details in Refs. 70, 71. The schematic diagram and some measures of the Helsinki setup are shown in Fig. 5. Both timing gates are most often used in such a way, that electrons emitted backwards after ion penetration through a thin carbon foil (5–22.9 μg/cm^2 in T_1 and 10–21.6 μg/cm^2 in T_2) are accelerated and guided by means of an electrostatic mirror to micro-channel-plates (MCP) where they are multiplied. The electron production and its influence on TOF detection efficiency will be discussed in more detail in section 4.2. The electrons are collected to an anode, and the anode signal is directed to a constant fraction discriminator (CFD). It transforms the negative pulse into a sharp edged logic timing signal. The timing signals from both timing gates are directed into a time-to-amplitude converter (TAC), which transforms the time difference of pulses into an output amplitude.

Ion implanted detectors from the Ortec Ultra series and Canberra PIPS series (active area 300 mm^2 and depletion depth 300–500 μm) were used as the energy detectors. After having been exposed to tens of millions of heavy recoils and scattered incident ions, the radiation damage in

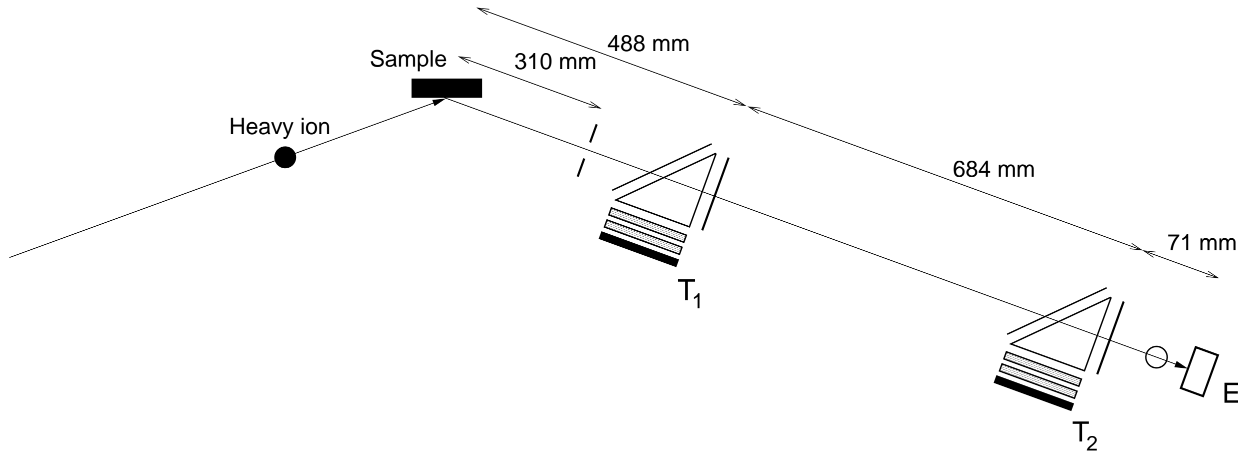

Figure 5: Schematic picture of the TOF-ERDA setup. The solid angle of the system, 0.18 mSr, is restricted by the circular aperture (18 mm in diameter) of the frame of the carbon foil in the second timing gate (T_2), located at 1172 mm from the sample. The solid angle of the first detector is reduced with an extra aperture (7 mm in diameter) located at 310 mm from the sample to reduce the amount of insignificant counts (outside T_2 solid angle, electron induced, etc.) in the first timing gate.

the detector deteriorates the energy resolution and increases the leakage current. In contrast to surface barrier detectors, ion implanted detectors can be annealed (2 hours in air at 200°C) and their original performance restored. A normal preamplifier (Ortec 142) and an amplifier (Tennelec TC 242) chain was used to amplify analog pulses, and both time and energy pulse-height signals were converted into digital ones in Canberra analog-to-digital converters (ADC) and recorded with a Canberra MPA/PC multiparameter system.

In most of the existing TOF-ERDA setups the signal from the first timing gate is delayed for a few hundred nanoseconds, and the signal from the second gate is used as a start signal. This arrangement is motivated by the lower false event count rate of the second detector. On the other hand, long delay cables increase the noise in the TOF detector and degenerate the TOF resolution. This was tested by taking delayed TOF, direct TOF, and energy signals at the same time. Direct TOF signals are used today because they have a better time resolution and no events are lost at normal count rates (less than 1000 Hz). The situation would be different if the count rate of false events were higher at the first timing gate, for instance due to the aging of the MCP.

An example of TOF-E data is shown in Fig. 6. The data is from a study in which the time and temperature dependency of the proton exchange in $LiNbO_3$ was studied [34]. This optical wave guide material was measured using 58 MeV $^{127}I^{11+}$ ions. Fig. 6a shows the projection of the histogram in Fig. 6b to the TOF axis. Fig. 6c shows a low energy area magnification of the energy-axis projection in Fig. 6d. The measurements were done in the coincident and non-coincident modes. TOF and E events appearing at a maximum of 2.1 μs from each other were collected in coincidence and the events outside this limit where marked as non-coincident events.

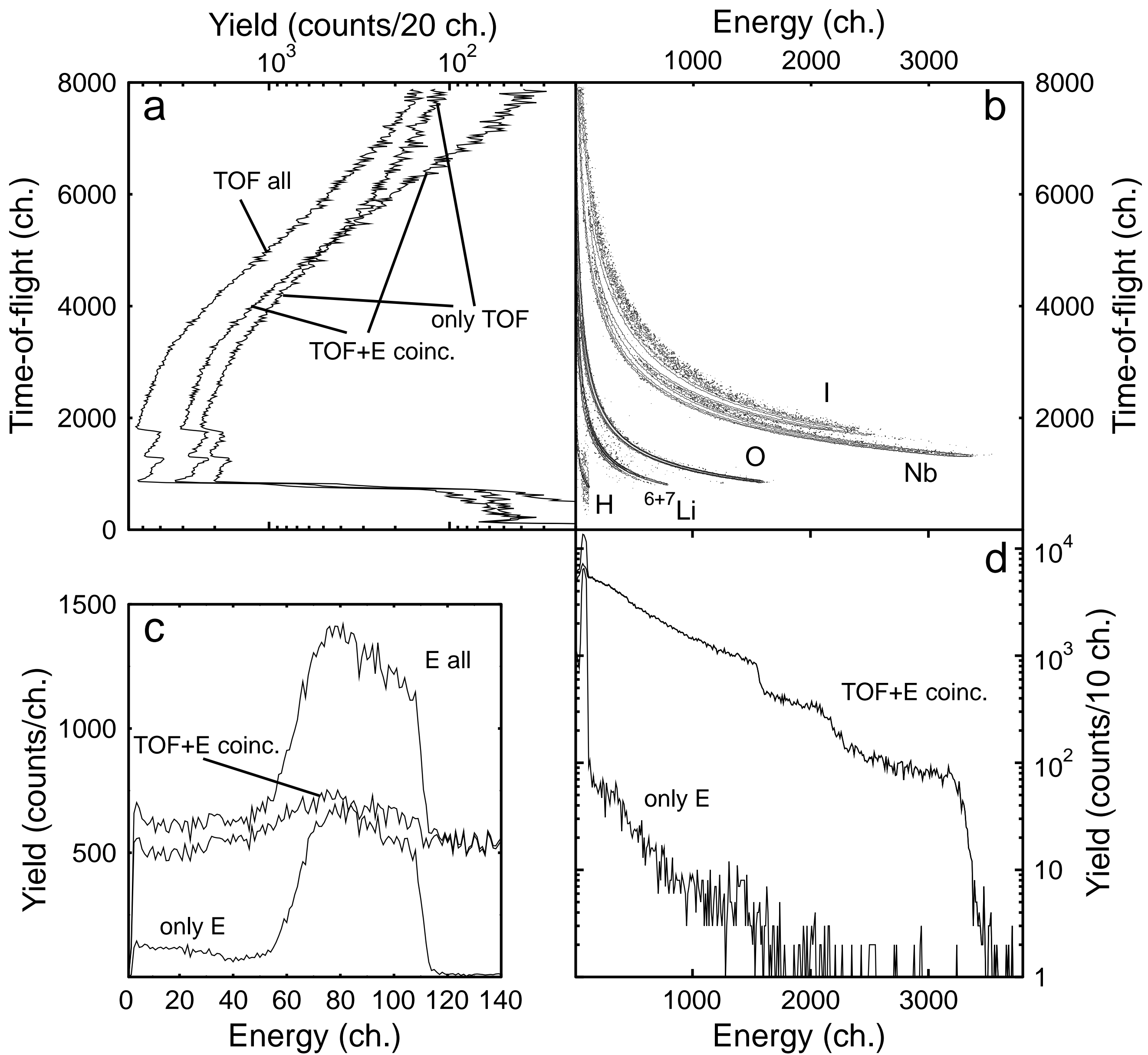

Figure 6: Coincident events in energy *vs*. time-of-flight histogram (b) from a proton exchanged $LiNbO_3$ sample measured with 58 MeV $^{127}I^{11+}$ ions. In (a) a projection of the data in (b) to the TOF-axis (TOF all) is shown. Coincident events with the E detector (TOF+E coinc.) and the events observed only by the TOF detector (only TOF) are drawn with separate lines. In (d) the projection of the data in (b) is made to the E-axis. In (c) the low energy region of (d) is enlarged to show the hydrogen signal more clearly. Note the logarithmic y-scales in (a) and (d).

As can be seen in Fig. 6a, the ratio between the coincident TOF+E events and the non-coincident TOF (only TOF) events remains constant at high energies (short time of flights) but for long time of flights the number of non-coincident events is increased. For this particular sample, the explanation is mainly the low energy Li and O events which are observed by the TOF detector but not by the energy detector. One reason for this is multiple scattering (see section 6.4), but it is mainly

due to the low energy discrimination of the energy detector. The ratio of the short flight times is proportional to the ratio of the solid angles of the aperture in front of the first timing gate and aperture carrying the carbon foil in the second timing gate.

As can be seen in Fig. 6d, the number of non-coincident events in the energy detector (only E) is very low for heavy elements and high energies. However, for hydrogen the TOF detection efficiency is strongly energy dependent (as is discussed in more detail in section 4.2) and the amount of non-coincident events is high.

4.2 Detection efficiency

The ERDA techniques combined with a TOF-E telescope provide a very useful tool for quantitative elemental depth profiling for all the elements in almost any matrix. The detection efficiency of our TOF-E telescope was studied in paper I. This section presents the main results obtained and some further studies closely related to detection efficiency.

4.2.1 Electron emission and multiplication

In an ideal TOF-E telescope every ion within the solid angle of the detector creates a signal in the timing gates and the energy detector. For light element recoils this is restricted by the detection efficiency of the TOF detector lower than 100%. This is due to the low electron emission in the carbon foils of the timing gate. For H and He ions the electronic stopping powers are so low that only a few electrons are emitted from the carbon foils [72]. One possible solution to step up the electron emission is to increase the thickness of the carbon foil. As observed by Koschar *et al*. [73], the secondary electron yields for 12 MeV ^{12}C ions are saturated for carbon foil thicknesses over 15 μg/cm^2. However, at the thickness of 5 μg/cm^2 the electron emission reaches 80% of its maximum for 12 MeV ^{12}C ions. In addition to energy loss, electron emission is also dependent on the charge state of the passing ion. In the research for this thesis the thinnest carbon foils used were 5 μg/cm^2 thick. The same detection efficiencies were obtained for them as for 22 μg/cm^2 thick foils. Also much thinner carbon foils have been used by other groups [68, 74, 75], but the films were diamond-like carbon (DLC) films.

In Fig. 7a the dependency of the detection efficiency on the electronic stopping power is plotted for light ions. The detection efficiency of the charged particle detector is presumed to be 100% in the energy range of this study. According to the Sternglass theory [76], the mean number of ejected secondary electrons is proportional to the electronic stopping power. The relation between the MCP signals and stopping power can be seen in Fig. 7b, where the MCP signal height and stopping power are plotted as a function of the energy of ^{11}B ions passing the carbon foil. When compared to the SRIM2000 stopping power of carbon for ^{11}B, the shape of the MCP signal is narrower and the maximum is at a much lower energy. The energy dependency of the measured MCP signals agrees

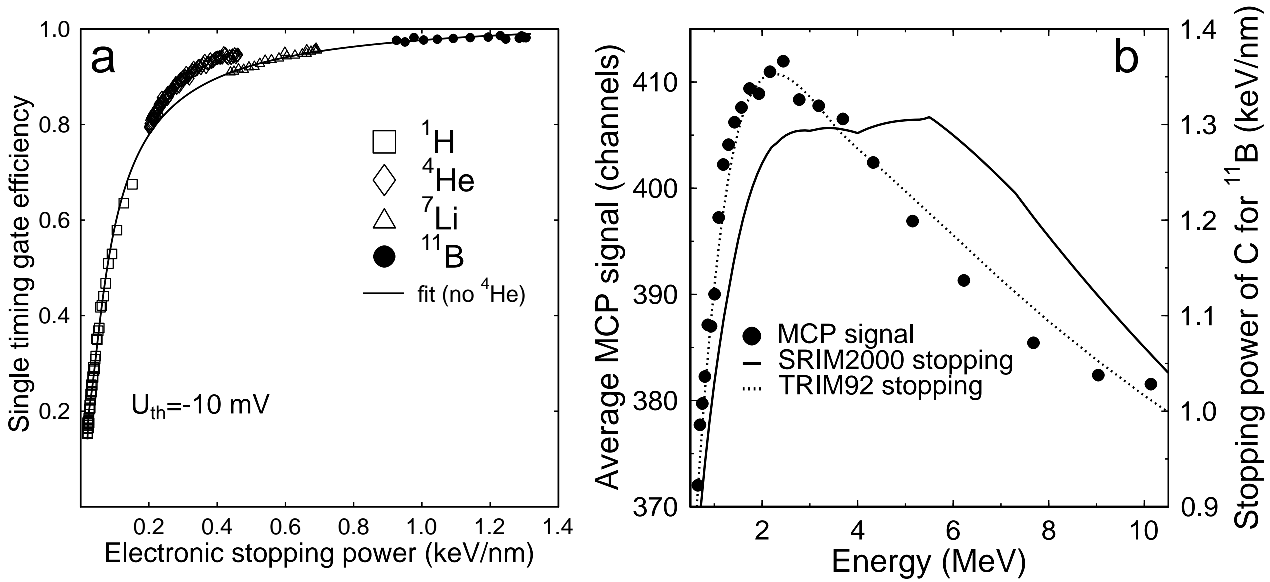

Figure 7: Detection efficiency of a single timing gate for H, He, ^{7}Li, and ^{11}B ions as a function of the stopping power in carbon (a) [I]. The discrepancy of the He detection efficiency and the fit is due to the MCP change before the He measurements. In (b) the MCP signal height is plotted as a function of ion energy dependency for ^{11}B ions together with the SRIM2000 and TRIM92 stopping powers of C for ^{11}B ions [38]. The different y-axis scales were fitted with each other in (b).

very well with the older TRIM92 stopping power data for ^{11}B ions in carbon. Some TOF-ERDA measurements for this thesis were performed having both timing gates rotated by 180°. Although the electron emission is almost doubled in the forward direction [77], the detection efficiency for hydrogen increased only by a few per cent.

In addition to the secondary electron emission, there are also other factors that affect the detection efficiency of the TOF detector. The electrons emitted have to pass three grids with an overall optical transparency of ∼0.85 before reaching the first MCP. The MCP has a quantum efficiency determined by the active area of the channels (∼0.4–0.6) and the probability that an incident electron creates one or more secondary electrons when hitting a channel wall. This electron multiplication is governed by the bias voltage applied over the MCP. For instance, a 50% increase in the detection efficiency for hydrogen was observed when a voltage of 990 V (U_{T_2}=6.8 kV over all T_2 detector) was applied over one MCP instead of the normally used voltage of 900 V (U_{T_2}=6.2 kV). A drawback of the higher bias voltage is the shorter life time of the MCP stack due to aging induced by larger electron clouds and sparking. More than 1500 separate measurements have been performed during the past three years without an MCP change using the bias of ∼900 V. The voltage dependency of the electron multiplication is illustrated in Fig. 8a. Because of the low electron yields the detection efficiency for ^{15}N ions starts to drop when the MCP voltage is below 800 V (U_{T_2}=5.6 kV) as illustrated in Fig. 8b.

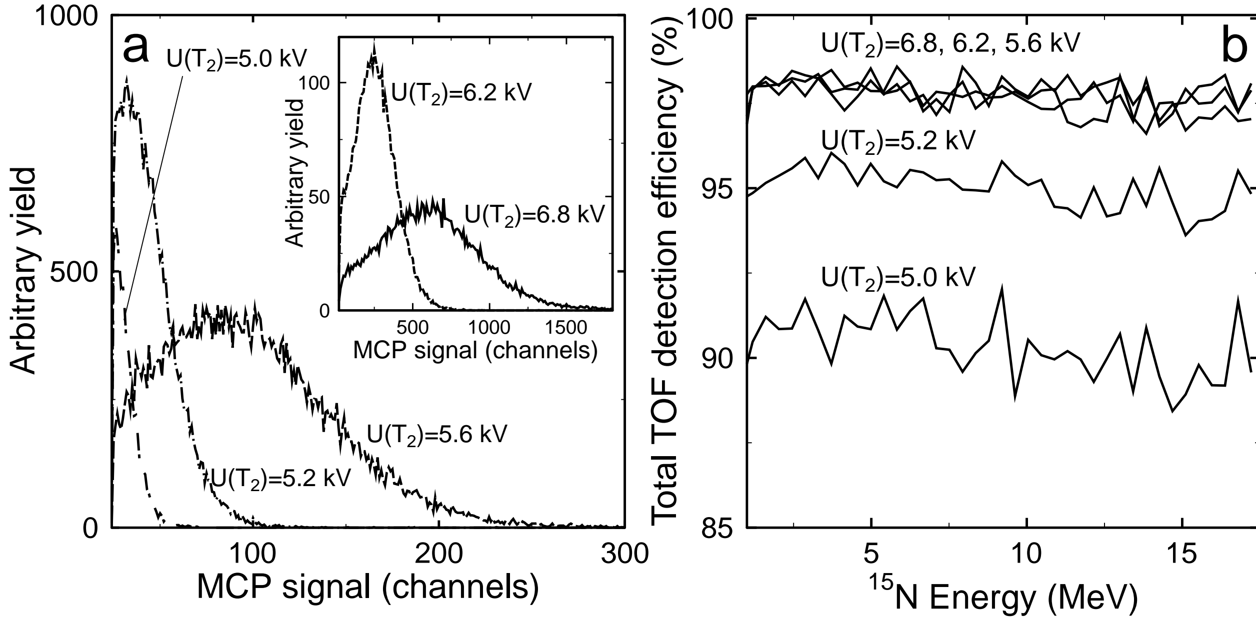

Figure 8: MCP signal heights collected from the anode for the 5–10 MeV energy range of ^{15}N ions scattered from a gold target for different voltages applied over T_2 timing gate (a). A voltage of U_{T_2}=6.2 kV corresponds to a single MCP voltage of ~900 V. In the insert the MCP signal heights are plotted for higher voltages. The corresponding energy dependent detection efficiencies are plotted in (b). The T_1 voltage was kept at 6.2 kV. The MCP signal height was collected from T_2 by feeding a minute fraction of the anode pulse through a resistor (56 kΩ), preamplifier, and amplifier, while letting the main part of the signal go to the CFD.

4.2.2 Discriminator threshold

After being multiplied in the two MCPs, the electrons are collected from the anode and the generated negative pulse is directly fed into a CFD. A more common arrangement used in the literature is to amplify the signal before the CFD [46, 64], but we did not find it useful as the pulses were high enough such as they were.

The threshold level of CFD is the next factor limiting the detection efficiency. The threshold should be set as low as possible. For this thesis the lowest possible discriminator setting of -10 mV was used and no harmful background signals were observed during the measurements. In Fig. 9 the MCP signal spectrum is plotted for different threshold levels of -(10–400 mV) for 17 MeV ^{15}N ions passing the telescope. The MCP signal was measured in coincidence with TOF and E. A clear cut can be observed in low MCP signal heights as a function of threshold voltage. This causes loss of events and decreases the detection efficiency.

In Fig. 9 an MCP signal measured in coincidence only with the TOF signal (MCP-TOF coincidence) is plotted (U_{TH}= -10 mV). For large MCP signals the yield is uniform with the spectra obtained in the TOF-E-MCP coincidences but a significant peak can be observed at the low signal

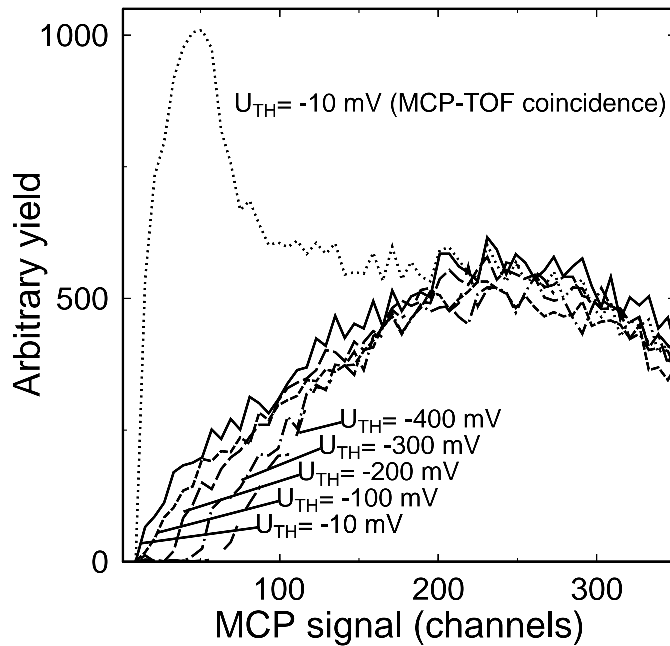

Figure 9: MCP signals from T2 as a function of the CFD threshold -(10–400) mV for 17 MeV ^{15}N ions. For the lower curves the condition of the TOF–E–MCP-coincidence was fulfilled, in the upper curve only the TOF–MCP-coincidence,

heights (channels below 100). The peak originates from events that do not produce signals in the energy detector and for 17 MeV ^{15}N ions they are mostly due to ions hitting the metal frames holding the carbon foil in the second timing detector. In addition to the ions hitting the metal frame, the low height MCP signals from H and He ions can be observed from the anode without triggering the CFD, which has a threshold voltage of -10 mV. These events are detected in the energy detector as non-coincident events.

The detection efficiency of the TOF detector is not entirely related to the secondary electron ejection and the CFD signal detection. For heavy recoils the scatterings in the first carbon foil drop the detection efficiency when the recoils are scattered outside the solid angle of the second timing detector. This phenomenon modelled with the MC simulations [II] is discussed in more detail in section 6.4. In general, the detection efficiency related difficulties affect the measurements of H and He. To minimise the detection efficiency fall for low energy heavy ions, thin carbon foils should be used especially in the first timing gate.

4.3 Hydrogen analysis

A low detection efficiency for hydrogen is a serious problem for TOF detectors [62, 65, 78] because hydrogen is one of the most regular and crucial impurities in thin films and semiconductor materials. Therefore, much effort has been expended to detect it with different ion beam analysis methods.

A method used extensively for hydrogen detection is nuclear reaction analysis (NRA) utilising the reaction $^{1}H(^{15}N,\alpha\gamma)^{12}C$. This is a very sensitive method with a good depth resolution for hydrogen profiling [79–81]. Yet a determination of the absolute hydrogen concentration requires the use of hydrogen standards and detailed measurements are time-consuming.

For the detection of hydrogen in TOF-ERDA measurements a charged-particle detector specific to hydrogen profiling has been used [82]. Undesired recoiled and scattered ions are avoided by placing an absorber foil in front of the detector. Such an absorber thickness is chosen that only light ions can pass the foil. A drawback of this method is decreased energy resolution due to the energy straggling of ions in the absorber foil.

A setup consisting of a transmission energy detector (ΔE) and a residual energy (E) detector can be used as was done by Wielunski *et al*. [83]. As the energy loss in the ΔE detector is isotope dependent, different isotopes can easily be separated by plotting the events in a ΔE,E histogram. If a light projectile like He is used, the low stopping power deteriorates the depth resolution to 40–50 nm depending on the matrix [83]. For quantitative results, this setup requires the use of a standard sample with a known hydrogen isotope concentration or simultaneous RBS measurements [83].

Another common approach is to measure the detection efficiency of a TOF detector for different elements and use the efficiencies to normalize the measured energy spectra for hydrogen [84]. No additional detector is required and the normalization is easy to do. However, as the efficiencies for high-energy H ions can be quite low (<10%), the counting statistics becomes a problem. In addition, any change in the detection efficiency affect the determination of the hydrogen content. The detection efficiency can change for instance due to the aging of the MCPs and drift in the high voltages applied to the timing gates.

A highly improved method was developed for this thesis. It resembles an approach which combines charged-particle and gas-ionisation detectors [56–60]. The main idea behind it becomes evident from Fig. 6c. Instead of only measuring the coincident events of the TOF and energy detectors, the data are selected to include also the non-coincident events. By taking advantage of the fact that the TOF detection efficiency for other recoils than hydrogen is close to 100%, the non-coincident events in the energy detector are mainly from hydrogen recoils. By adding the coincident and non-coincident events a 100% detection efficiency is obtained for hydrogen. However, another condition has to be fulfilled: the maximum flight time has to be long enough for even the low energy heavy recoils and scattered ions to traverse the flight path during it. In our detector with the flight path of 684 mm, a 500 ns wide time window was found to be suitable. A broader time window would create noise events and limit the count rate. Too narrow a time window would leave low energy heavy ions

Table 1: Round Robin: Measurement of H implants in silicon by ERD [85].

Laboratory	Beam used	Method	Detector	Standard	H content 10^{15}at/cm^2 tot.	surf.	impl.	Error estimate of impl. H % prec.	acc.
Canberra	200 MeV ^{197}Au	ERD	GID[1]	Si stopp.	64	–	–	1.7	6
London	1.6 MeV ^{4}He	ERD	Si, 6μm Mylar absorber	Kapton Mylar	69.4	10.4	59	3.4	>5
Surrey	1.5 MeV ^{4}He	ERD	Si, 6μm Mylar absorber	Kapton	71.6	14	57.6	2.6	6
Helsinki	**53 MeV ^{127}I**	**ERD**	**TOF–ERD**	**Si stopp.**	**61**	**5**	**56**	–	**5**
Rossendorf	6.4 MeV ^{15}N	NRA	NaI	Kapton	63.3	6.3	57	4	–
	35 MeV ^{35}Cl	ERD	Si, 18μm Al foil	impl. ^{2}D	66	–	–	4	–
Montreal	40 MeV ^{63}Cu 30 MeV ^{35}Cl	ERD	Si, 13 μm Mylar + 17 μm Al abs.	Si stopp.	–	–	55.5	1.8	–

[1] Gas ionisation detector

outside the time window, and they would appear in the energy detector as non-coincident counts in the hydrogen region of the energy spectrum, thereby disturbing the hydrogen analysis. In Fig. 6c the high background in (TOF+E coinc.) signal is due to other coincident signals in energy channels. When the coincident hydrogen events are selected from the histogram and added to non-coincident energy detector events, almost background-free energy spectrum is obtained.

The method for hydrogen detection was tested in a Round Robin experiment [85]. A silicon wafer was implanted with 6 keV protons to a nominal fluence exceeding 5×10^{16} at./cm^2 and a uniformity better than 2% over the wafer. The samples were analysed in leading ion beam analysis laboratories doing ERDA. The results are presented in Table 1. The average value of the implantation fluence was determined to be $5.70\pm0.14\times10^{16}$ at./cm^2. The inter-laboratory reproducibility (1 σ) was found to be 2.5% which is better than the individual error estimates suggest. In our results the inaccuracy originates mainly from the difficulties experienced in resolving the surface hydrogen peak from the implanted distribution. Because we did only one measurement, no precision value was reported for our result. The loss of hydrogen in the surface peak during the analysis is discussed in detail in section 6.6.1.

Normalization with the known detection efficiency and the full detection efficiency methods were utilised in the ERD analysis of this thesis. The latter was found especially usable in the deuterium diffusion studies in paper IV and Ref. 29 and in a study of the proton exchange process in $LiNbO_3$ [34]. In paper VI the full detection efficiency method was applied for hydrogen detection in ALD deposited TaN thin films.

4.4 Forward scattering analysis

HI-ERDA is usually considered as a useful tool for the detection of light elements in heavy matrices. Heavy recoils do not get much energy from lighter probing ions and are very sensitive to multiple

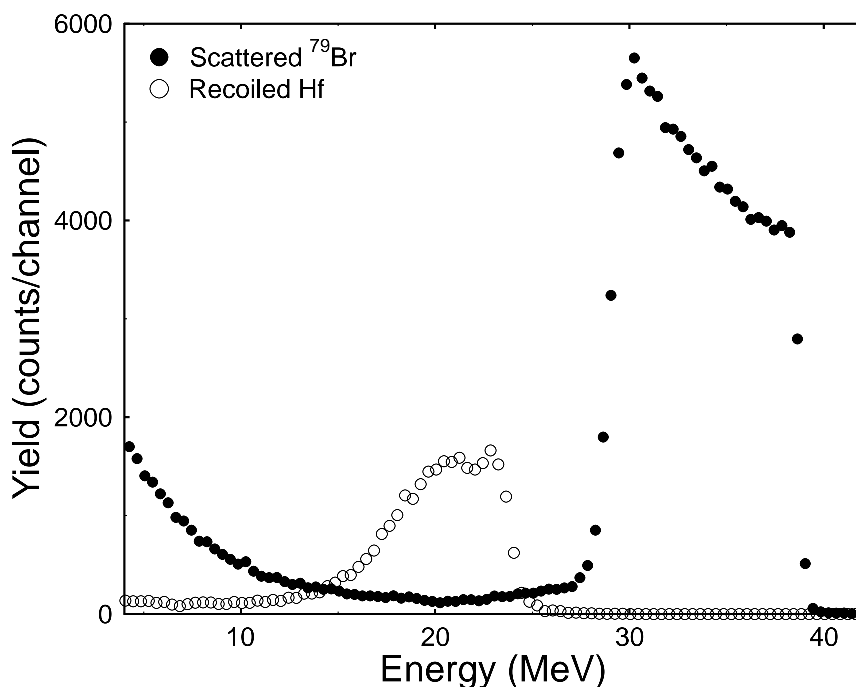

Figure 10: Forward scattered ^{79}Br and recoiled Hf ions from a 130 nm thick HfO_2 film on a silicon wafer [18]. The film contained also 1.6 at.% of Zr, which generates a low background (<1/50 of Hf) for scattered ^{79}Br at 24–31 MeV. In comparison with the Hf recoil spectrum, forward scattered ^{79}Br ions offer a much better resolution both at the surface and interface. The low energy tail due to the multiple scattering is clearly visible for scattered ^{79}Br.

scattering both in the sample and the TOF detector, as will be shown in section 6.4 and in Fig. 10.

However, when the concentrations of heavy sample atoms are to be solved, it is much more favourable to include both scattered incident ions and recoils in the analysis. In the analysis of heavy atoms in many oxides (*e.g.* TaO_2, Ta_2O_5, HfO_2) and nitrides (*e.g.* TaN) it is favourable to use forward scattered ions. Normally no disturbing main constituents or impurities are detected and the detected scattered ions result entirely from scatterings with the heaviest sample atoms. Due to the poor mass resolution of TOF-ERDA for heavy masses, mass separation cannot be done in all cases, for instance between ^{197}Au projectiles and ^{181}Ta recoils. In the analysis of TaO_2, TaN, and HfO_2 the use of ^{127}I and ^{79}Br ions and the utilisation of scattered projectiles in the analysis makes a thorough characterisation of all the sample elements possible. The experimental energy spectra of scattered 48 MeV ^{79}Br ions and Hf recoils are presented in Fig. 10 for a 130 nm thick HfO_2 thin film. The higher yield due to the larger scattering cross-section and the smaller multiple scattering distortions favour the use of scattered ^{79}Br ions in the analysis.

An important drawback of using both recoils and scattered ions in the same analysis is the different angle dependency of the scattering cross-section for these two processes, as is shown in Fig. 3b. Therefore an accurately known detector angle is required. An error of one degree (for instance 39°

Table 2: Concentrations (at.%) obtained in RBS and TOF-ERDA measurements of $LaGaO_3$ [86] and $Cu_xIn_ySe_z$ [V] thin films. For the scaling of the RBS results the light impurity amounts measured with TOF-ERDA were used.

$Cu_xIn_ySe_z$

Method	Se	Cu	In	H	O	S	C	N	K
RBS	30±1	18±1	14±1	–	–	–	–	–	–
TOF–ERDA	30±3	18±3	14±3	11±3	10–15	5.0±0.5	5.0±0.5	5.0±0.5	0.5±0.2

$LaGaO_3$

Method	La	Ga	O	Cl	C	F
RBS	20±1	22±1	58±4	0.4±0.2	–	–
TOF–ERDA	19±2	19±2	62±3	0.7±0.1	0.4±0.1	0.3±0.1

instead of 40°) would yield to a ratio of O:Ta = 1.74 instead of stoichiometric TaO_2 (Eqs. (6) and (5)). The detector angle used in this thesis was determined to be 40.0±0.1° by comparing yields of scattered ^{127}I and recoiled Ce from 50 nm thick CeO_2 films [17].

The use of heavy forward scattered ions in a standard analysis broadens the application field of TOF-E detectors. In the analysis of thin films it is not only a complementary but also substituting alternative for RBS analysis. In the analysis of TaN thin films in paper IV the use of scattered ^{127}I for Ta concentration determination proved to be very successful even in the analysis of very thin films (<50 nm). The scattered projectiles were also used in the analysis in Refs. 15, 16, 18, 19, 22.

5 COMPLEMENTARY MEASUREMENTS

In addition to TOF-ERDA, several other thin film characterisation methods were utilised for this thesis. The most important and used ones are discussed below.

5.1 Nuclear reaction analysis and Rutherford backscattering spectrometry

A variety of characterisation methods have their origin in the utilisation of interactions between colliding nuclei. These interactions can be divided into two main groups based on (i) the Coulomb repulsion force and (ii) nuclear force. RBS and ERDA belong to group (i).

When the Coulomb interaction takes place within the closest electron radius, the ion-atom interactions can be understood through the equations given in section 3.2. If the energy of an incident ion is not high enough to penetrate through the closest electron shells, the Coulombic repulsion of the nuclei is shadowed by the electrons and the scattering cross-section deviates from the Rutherford cross-section.

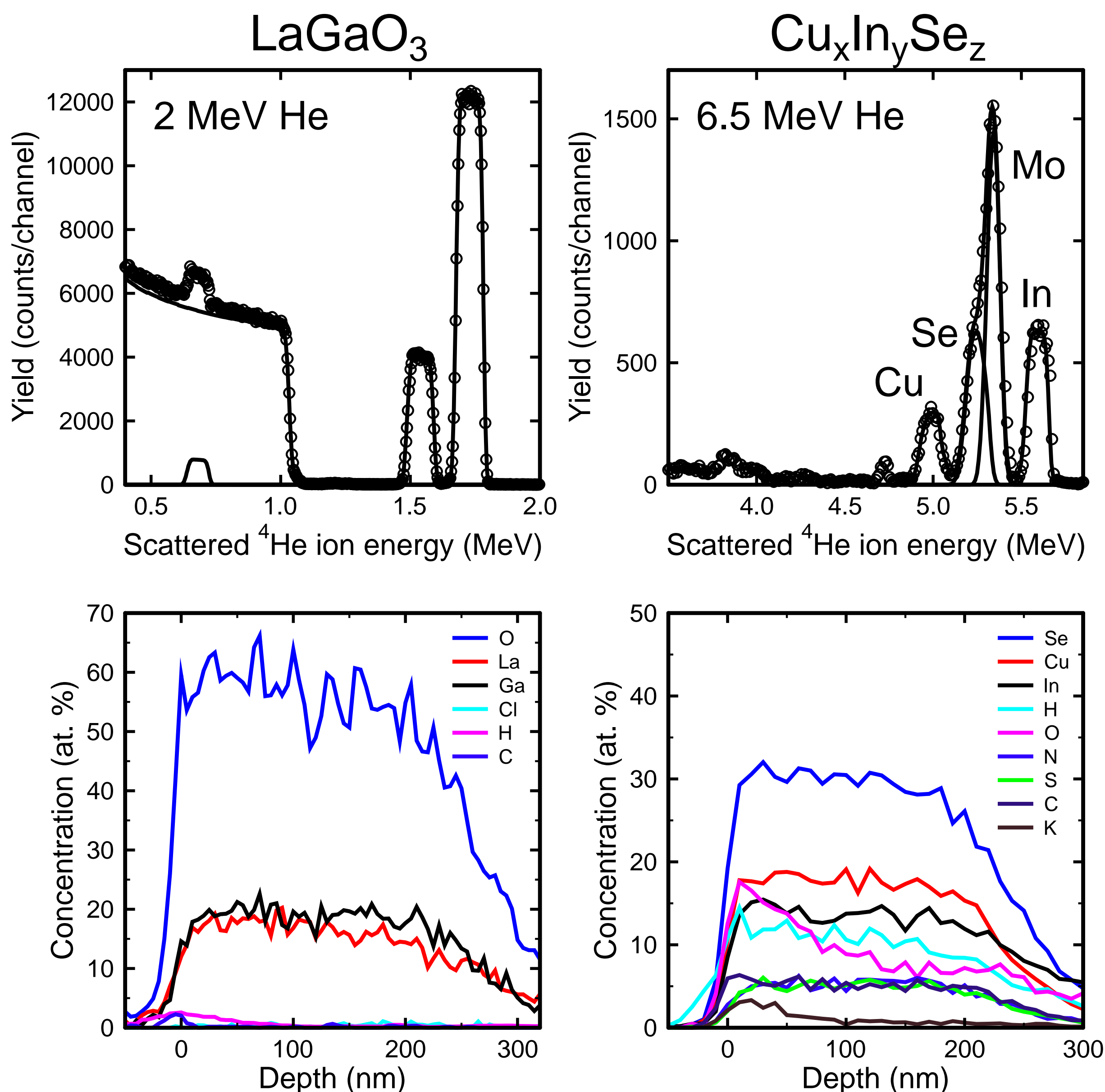

Figure 11: RBS energy spectra of $LaGaO_3$ [86] and $Cu_xIn_ySe_z$ [V] thin films (above) and corresponding TOF-ERDA depth profiles (below) measured with 48 MeV ^{197}Au ions.

In interaction (ii), the incident ion energy is so high that the projectile and the target nuclei approach within the range of nuclear forces and Rutherford formula again fails to describe the interaction. The projectile can excite the target nucleus to a higher energy state and, at even higher energies produce nuclear reactions.

In nuclear reactions much used for accelerator based depth profiling, two interacting nuclei form a compound nucleus. It deexcites by emitting γ-rays, protons, neutrons, alpha-particles, etc. which are detected. For quantitative determinations particle-gamma reactions are favoured. The reaction ^{1}H(^{15}N,αγ)^{12}C at 6.39 MeV is widely used for hydrogen depth profiling. The incident ion energy

is changed in the vicinity of a very narrow resonance at 6.39 MeV (full width half maximum 120±30 eV [87]), and the amount of emitted 4.43 MeV gamma rays is detected as a function of energy (depth) [79]. For particle-particle reactions, deuterium induced reactions are ones mostly used in backscattering geometry; with them low concentration levels of light elements (from ^{2}H to O) can be detected. In all nuclear reaction methods a well characterised standard is needed and careful incident ion fluence repetition is required for exact quantification.

In RBS, only the backscattered probing ion is detected, and the depth in which the scattering had occurred can be calculated by means of scattering kinematics (Eq. 2) and stopping powers. In a typical measurement geometry the energy detector is at an angle of 170° and the sample normal direction tilted 175° with respect to the incoming beam. When homogeneous thin films with all film elements detectable are measured, atomic concentrations can be calculated from the backscattering yields according to the Rutherford scattering cross-sections, see Eq. (6). Moreover, the stopping cross-sections of many materials for most commonly used hydrogen and helium ions are experimentally well known.

Complementary RBS spectra and TOF-ERDA depth profiles of $LaGaO_3$ [86] and $Cu_xIn_ySe_z$ [V] thin films are presented in Fig. 11. The atomic concentrations of the same samples are presented in Table 2. For this thesis, RBS was used in papers III,V, and VI, and in Refs. 20, 21, 27, 32, 33.

5.2 Other thin film characterisation methods

5.2.1 Secondary ion mass spectrometry

Secondary ion mass spectrometry (SIMS) is a very sensitive depth profiling method for all elements in a sample. In SIMS a focused ion beam (Ce^+ or O_2^+) is used to erode the studied sample and the yields of different emitted sample ions are measured as a function of time. The time scale is converted to a depth scale by measuring the depth of the produced crater and assuming a constant erosion rate. SIMS is a very powerful tool for diffusion studies and depth profiling of low concentrations (below ppm levels) in homogeneous samples. For quantitative analysis, the use of either specially prepared standard samples, for instance ion beam implanted [32], or well characterised samples is required. In paper VI and Refs. 29, 30 the concentrations measured by TOF-ERDA were used to normalise the SIMS results. This is illustrated in Fig. 12 in which both TOF-ERDA and SIMS deuterium depth profiles in Si doped DLC films (33 at.% Si) are presented [VI]. In the TOF-ERD analysis of the deuterium content the method described in section 4.3 was used.

5.2.2 Scanning electron microscopy

Scanning electron microscope (SEM) combined with energy dispersive X-ray detection (SEM-EDX) has a wide dynamic scanning range, and its easy usage has made it a basic tool in materials

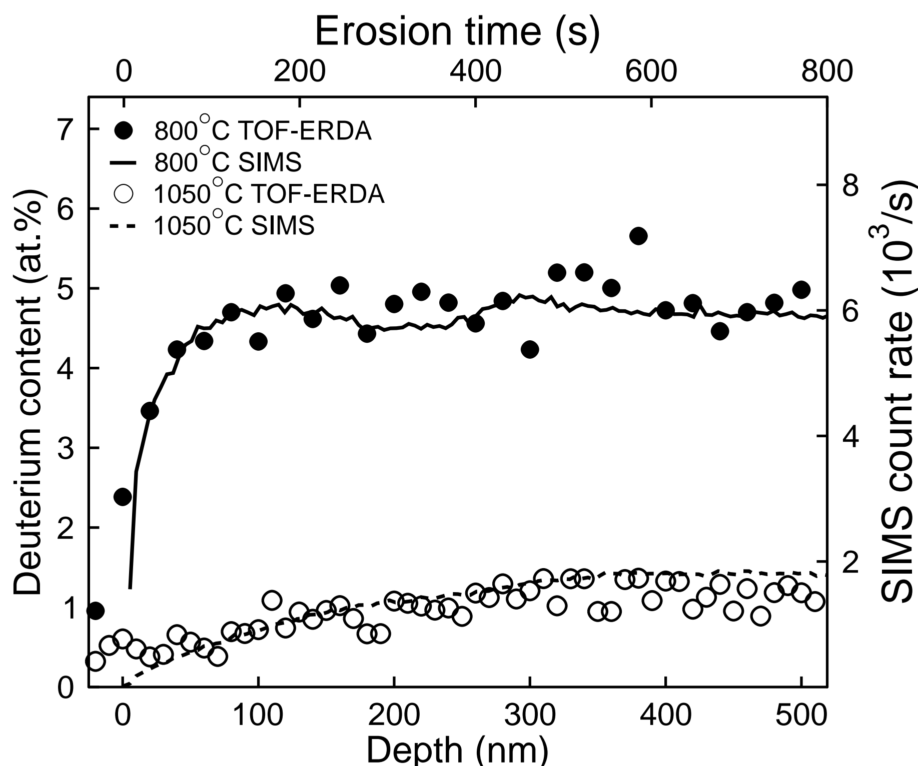

Figure 12: TOF-ERDA and SIMS depth profiles of deuterium in Si doped (33 at.% Si) diamond-like carbon films [VI]. TOF-ERDA results were used to normalise SIMS depth profiles.

characterisation. In SEM-EDX high energy electrons (5–30 keV) excite the sample atoms when hitting the sample and emitted characteristic X-rays are detected with a semiconductor detector. By means of standard samples, a quantitative concentration analysis can be performed for elements heavier than C for a homogeneous thin film. Light impurities remain undetected, and the measurement of insulating samples requires the usage of a thin conducting layer on the top of the sample. SEM-EDX has been used in papers V and VI, and Refs. 8, 13, 20, 22, 23, 31.

5.2.3 X-ray photoelectron spectroscopy

In X-ray photoelectron spectroscopy (XPS) or electron spectroscopy for chemical analysis (ESCA) the sample surface is irradiated with X-rays and surface atoms emit electrons after direct energy transfer to the electrons. The electron energy is measured, and the emitting atom (except H and He) can be identified from the characteristic electron energy. Furthermore, the high energy resolution of the electron spectrometer makes it possible to obtain chemical information of the atomic bonds. With ion etching, elemental depth profiles can be obtained to a depth of hundreds of nanometres like in SIMS. XPS was utilised in Refs. 10, 11, 13, 21, 25.

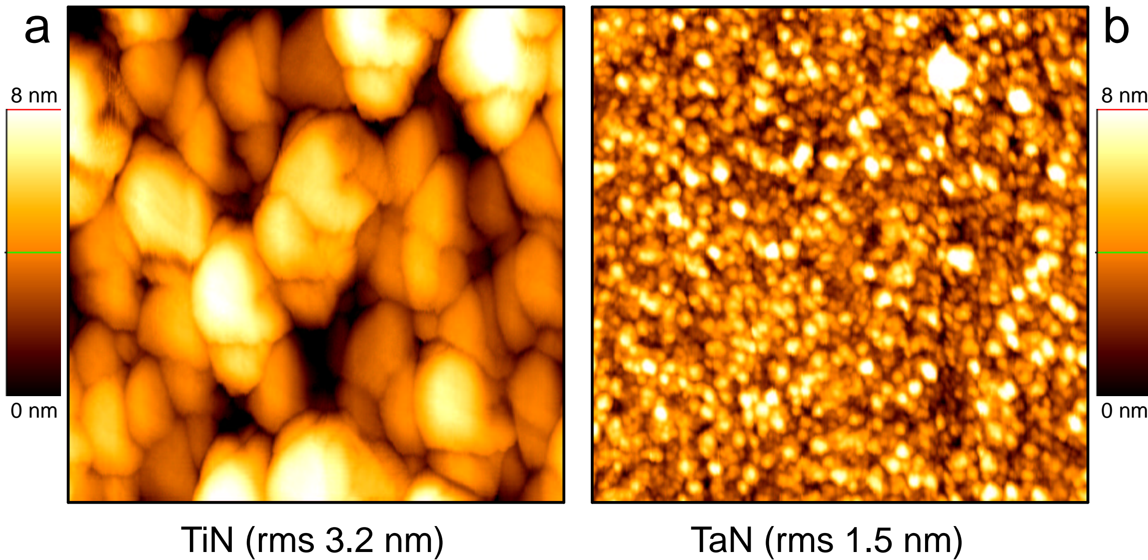

Figure 13: STM (a) and AFM (b) images from potential diffusion barrier materials TiN and TaN grown by ALD. The lateral scale in (a) is $0.5\times0.5\ \mu\text{m}^2$ and in (b) $1\times1\ \mu\text{m}^2$. In STM image the tip shape is reproduced in the higher grains instead of surface topography. The conductivity of the TaN film was too low to be measured with STM. The TOF-ERDA results from these films are presented in Table 3 on page 34.

5.2.4 Scanning probe microscopy

In STM a quantum mechanical phenomenon, quantum tunnelling, is utilised in surface characterisation. The basic idea in STM is to measure the tunnelling current between a tip and a sample, which are in different electrical potentials. The electrons have a finite possibility to penetrate through the potential barrier (a vacuum or dry air cap) between the materials. The strong distance dependency of the tunnelling current can be applied to surface characterisation if the two materials are moved laterally with respect to each other. In other mode of operation the current is kept constant and the height information is obtained from the z-piezo movements. An STM topography image of a 100 nm ALD-grown TiN thin film [23] surface is presented in Fig. 13a.

In addition to STM, Binnig *et al*. also invented AFM [6]. It became a much more versatile tool, however, when Meyer and Amer presented their simple probing method [88]. A diode laser beam is focused on the backside of the cantilever holding a tip and bounced to a position sensitive photodetector. Tip (and therefore cantilever) movement is corrected via a feedback loop and the reflected laser beam is kept at the same position with z-piezo movements. The surface topography can be obtained from these movements. Fig. 13b presents an AFM image of a 60 nm thick ALD-grown TaN thin film [22].

For this thesis, the Digital Instruments Nanoscope III of the Helsinki University of Technology and ThermoMicroscopes AutoProbe CP Research of the Accelerator Laboratory SPMs were used in both the STM and the AFM modes. The average grain size and an estimation of the crystallinity of

the grown film can be obtained from SPM images. In ion beam analysis, especially with glancing in-going and out-coming angles the information of the surface topography is crucial and the aid of AFM or STM is needed. SPM techniques were utilised in paper VI and in Refs. 10–14,17,19,21,24.

6 PROGRESS IN THE ANALYSIS PROCEDURE AND RESULTS OBTAINED

In addition to the basic physical principles of ERDA presented in section 3 and the measurement system optimisation described in section 4, there are several factors which have to be taken into account when the measured spectra are interpreted and the elemental concentrations deduced. The analysis procedure used in the Accelerator Laboratory in TOF-ERDA and an MC program, which assists in interpreting the analysis results, are described below.

6.1 Beam quality and measurement geometry effects

The energy calibration of the analysing magnet in the 5 MV tandem accelerator EGP-10-II of the Accelerator Laboratory is based on the 6.39 MeV resonance of the reaction ^{1}H(^{15}N,$\alpha\gamma$)^{12}C. The energy spread of the incident beam used in this study was of the order of 10 keV.

During this study additional steering plates were installed into the high voltage terminal of the accelerator. Originally the accelerator was planned only for singly charged protons. The electrodes in the second accelerating tube are tilted to form an inclined electric field to prevent electrons to be accelerated towards the positive terminal. When ions with higher charge states (above 7+) are used the same inclined field also steers the ions towards the electrodes, and the assistance of the new steering plates is needed to direct the trajectories of the high charge state ions through the accelerating tube and the analysing magnet. After the installation of the plates the maximum available incident ion energy was almost doubled for ERD measurements.

In the beam lines of the target hall, the maximum beam angular divergence ($\sim$0.1° full width at half maximum) is governed by a magnetic quadrupole situated at 5.8 metres before the target. The solid angle of the TOF telescope defines the width of the scattering angle θ=40.0$\pm$0.4°. The energy broadening due to the solid angle is overtaken by multiple and plural scattering of in-going and out-coming ions, if the recoiled ions originate from greater depth than first tens of nanometres [II]. The beam spot size (normally the in-coming beam cross-section is about 1.5$\times$3 mm^2) effect is insignificant for the energy resolution. During the measurements the beam spot location was monitored optically from a quartz located at the sample holder.

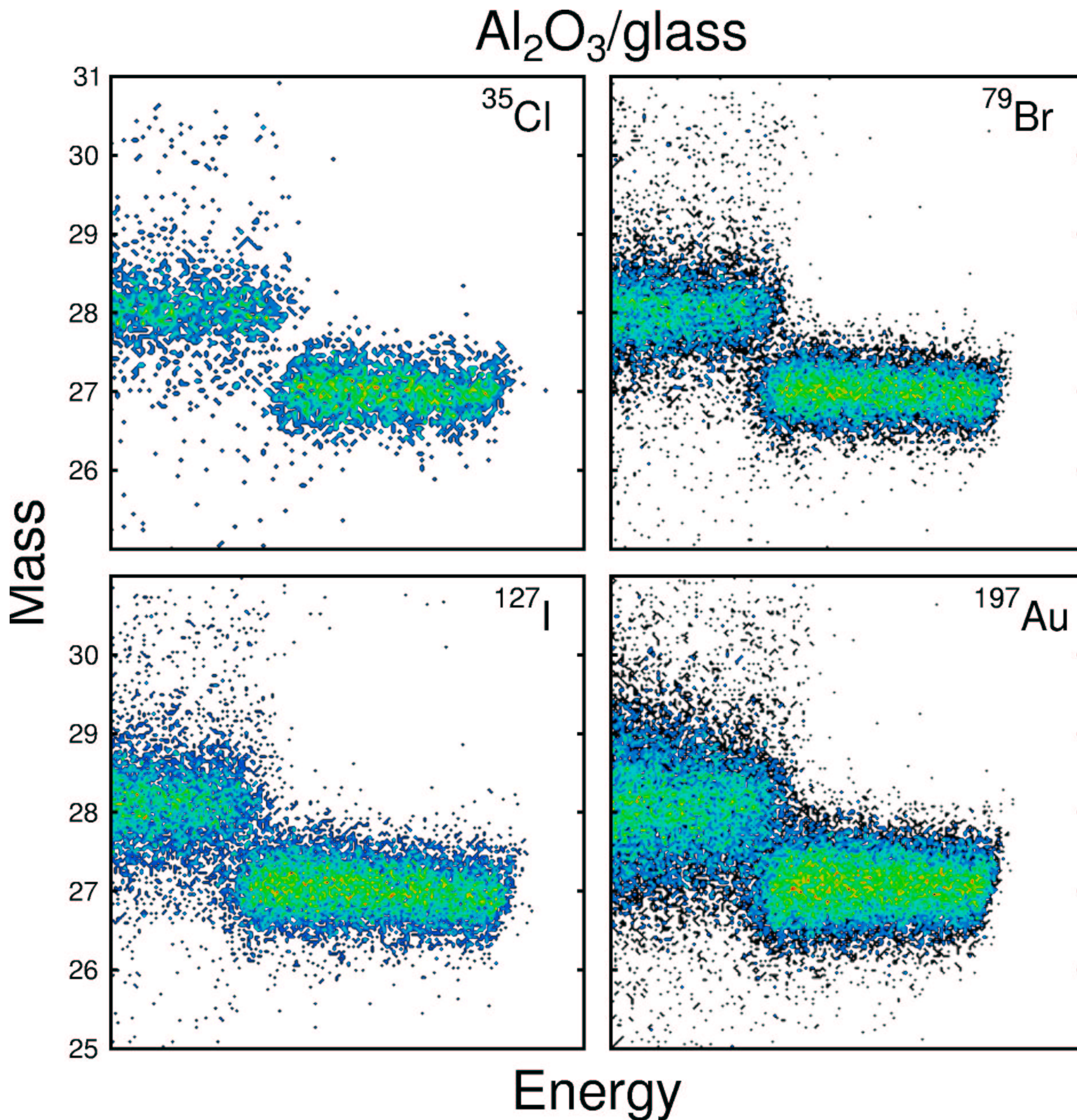

Figure 14: TOF-ERDA energy *vs*. mass histograms showing Al and Si recoils from a 170 nm thick ALD-grown Al_2O_3 film on a soda lime glass substrate measured with 43 MeV ^{35}Cl, 48 MeV ^{79}Br, 53 MeV ^{127}I, and 53 MeV ^{197}Au ions. Due to the scattering kinematics, a higher recoil energy leads to a better mass separation for light incident ions. For instance, the recoil energies for Al at the surface in a 40° scattering are 13.2 MeV and 24.8 MeV for 53 MeV ^{197}Au and 43 MeV ^{35}Cl ions, respectively. Every detected recoil is visible in the histograms and the energy scale is different in every histogram. The analysis results for different ions are presented in Table 3.

6.2 Selection of ions

The incident ions available from the different ion sources of the EGP-10-II range from hydrogen to gold. In most cases the highest energies possible are preferred in HI-ERDA because of the greater analysis depths, better mass separation, and smaller multiple scattering effects. To reach the high energies, ions with high charge states are required, and to obtain sufficient high beam currents for the analysis, high electron affinity elements are preferred. For example, the elements in the halogen group are especially suitable, because from them sufficiently high negative ion currents can be produced from the ion source. Most of HI-ERDA in the literature has been done with Cl, Br and I beams. Also Au has a high electron affinity and is much used.

We studied the suitability of different incident ions (43 MeV ^{35}Cl, 48 MeV ^{79}Br, 53 MeV ^{127}I, and 48 MeV ^{197}Au) in view of analysis and measurement fluency, accuracy, and ion induced irradiation effects in ALD-grown Al_2O_3 [89], TiN [23] and TaN [22] thin films. Desorption during the measurements and irradiation effects at the surface were studied for these ions. Additionally, 15°+25° geometry was studied for the mostly used 53 MeV ^{127}I ions. The results are given in Table 3. The elemental concentrations for TiN and TaN thin films were calculated directly from the number of events in the energy spectra by means of scattering cross-sections. This is stopping power independent approach (see section 6.3.2). An exception was oxygen, for which the concentration was obtained stopping dependently from the concentration distributions. For Al_2O_3 films the atomic concentrations were obtained from the concentration distributions. In the analysis of TiN and TaN with ^{35}Cl ions and TaN with ^{79}Br and ^{127}I ions the forward scattered incident ions were used in the analysis of Ti and Ta. The layer thicknesses were also determined from the depth profiles using the literature values for the film densities.

All incident ions employed were found feasible in the analysis of these films, although the low beam currents obtained for $^{35}Cl^{8+}$ ions required longer measuring times. On the other hand, 43 MeV ^{35}Cl ions give more energy to light recoils and improve their mass separation as is illustrated for Al and Si signals in Fig. 14. The concentration results measured with different incident ions were quite consistent for TaN and Al_2O_3. For TiN the origin of the high carbon content measured with ^{35}Cl ions remained unclear. The observed differences in other concentrations can be mostly explained by small discrepancies in the samples. In the thickness determination the errors can be thought to be due to the stopping powers [36] used. The given uncertainty estimates are obtained from the measurement statistics and the inaccuracies rising from ion beam induced desorption, which is discussed in more detail in section 6.6.1.

Table 3: TOF-ERDA results with different incident ions for ALD-grown Al_2O_3, TiN, and TaN thin films.

TiN/Soda lime glass†

beam	fluence (at./cm^2)	geometry	Ti	N	O⋆	Cl	C	d[1] (nm)
43 MeV $^{35}Cl^{8+}$	5×10^{13}	20°+20°	41±2	30±2	27	–	2.0±0.5	90
48 MeV $^{79}Br^{9+}$	3×10^{13}	20°+20°	43.1±0.6	28.1±0.6	27	0.10±0.03	0.40±0.08	75
53 MeV $^{127}I^{10+}$	1×10^{13}	20°+20°	45.6±0.6	27.2±0.6	27	0.11±0.03	0.47±0.08	80
53 MeV $^{197}Au^{10+}$	1×10^{13}	20°+20°	44.8±0.4	28.3±0.4	27	0.18±0.03	0.54±0.05	80

TaN/Soda lime glass†

beam	fluence (at./cm^2)	geometry	Ta	N	O⋆	Cl	Ti	C	d[1] (nm)
43 MeV $^{35}Cl^{8+}$	4×10^{13}	20°+20°	40±3	40±3	10	7‡	1.6±0.4	⊙	70
48 MeV $^{79}Br^{9+}$	1×10^{13}	20°+20°	43.2±0.3	38.6±1.3	10	5.5±0.4	2.1±0.2	0.4±0.2	55
53 MeV $^{127}I^{10+}$	2×10^{13}	20°+20°	41.0±0.1	39.9±0.8	10	7.7±0.3	1.3±0.1	0.37±0.07	60
53 MeV $^{127}I^{10+}$	5×10^{12}	15°+25°	41.9±0.3	38.3±1.0	10	7.9±0.4	1.6±0.2	0.14±0.03	65
53 MeV $^{197}Au^{10+}$	4×10^{12}	20°+20°	41‡	39.0±0.8	10	8.3±0.3	1.4±0.1	0.15±0.02	60

Al_2O_3/Soda lime glass

beam	flunce (at./cm^2)	geometry	O⋆	Al⋆	C⋆	H⋆	d[1] (nm)
43 MeV $^{35}Cl^{8+}$	1×10^{14}	20°+20°	60.6±1.2	37.8±0.7	0.14±0.02	1.4±0.2	160
48 MeV $^{79}Br^{9+}$	2×10^{13}	20°+20°	61.0±0.5	37.3±0.4	0.12±0.02	1.5±0.1	170
53 MeV $^{127}I^{10+}$	1×10^{13}	20°+20°	60.9±0.5	37.3±0.4	0.15±0.02	1.6±0.2	170
53 MeV $^{127}I^{10+}$	5×10^{13}	15°+25°	62.2±0.6	35.8±0.4	0.15±0.02	1.8±0.2	170
53 MeV $^{197}Au^{10+}$	6×10^{12}	20°+20°	61.5±0.4	36.5±0.3	0.17±0.02	1.8±0.2	160

† H concentration was below the detection limit.

⋆ Concentration was obtained from the depth profile.

‡ Concentration was obtained from measurements with other projectiles.

⊙ Concentration was below the detection limit.

[1] Densities 5.43 g/cm^3, 13.7 g/cm^3 and 4.0 g/cm^3 were used for TiN, TaN and Al_2O_3, respectively.

6.3 Concentration determination

In analysis where backscattering of ions is utilised the direct result is an energy spectrum from which the events originating from the scatterings with different sample elements can be distinguished by means of the kinematic factor (Eq. 2) and the stopping powers. Some preliminary information is often required (film constituents, thicknesses, light impurities) in detailed analysis. For element resolving techniques like TOF-ERDA, no a prori information about the sample composition is needed as different elements can be separated and selected according to their mass or atomic numbers as illustrated in Figs. 14 and 15.

6.3.1 Energy spectrum

In TOF-ERDA the mass calculation is based on the measured time of flight and energy for every recoil. However, the energy detector has a non-linear energy response for different heavy ions, and a higher order energy detector calibration has to be used [90]. Difficulties may also arise when mass overlapping occurs with the neighbouring elements as can be seen in Fig. 15 for scattered ^{127}I and recoiled Xe. Here Xe was an impurity in Ar gas used in a film deposition by magnetron sputtering. From these E-mass or TOF-mass histograms the events corresponding to different masses can be selected and the elemental energy spectra deduced from the TOF data. Normally the obtained energy spectra are not the final results, but they are used to further calculate the elemental concentrations.

6.3.2 Stopping power independent concentration determination

The stopping powers normally used [36] can differ as much as 20% from the correct ones [51]. Especially for heavy ions, the lack of experimental data is a problem, and therefore a stopping power independent approach gives more reliable results. The elemental concentrations of a thin film can be obtained by using the number of the recoil atoms or the scattered ions in the energy spectra and by calculating the ratios using Eqs. (5) and (6) for the recoil and scattering cross-sections, respectively. This approach can be used only if certain conditions are fulfilled: (i) The film has to be homogeneous, and no concentration peaks at the surface or interface are present. (ii) The detection efficiency for different elements has to be known, and correction parameters must be used, if necessary. (iii) The film should be relatively flat and thin to avoid low energy tails due to the roughness and multiple scattering. (iv) The substrate should not contain the same elements as the thin film on it. When these conditions are fulfilled, the uncertainty of the obtained concentration ratios arises almost only from the statistics of the detected recoils.

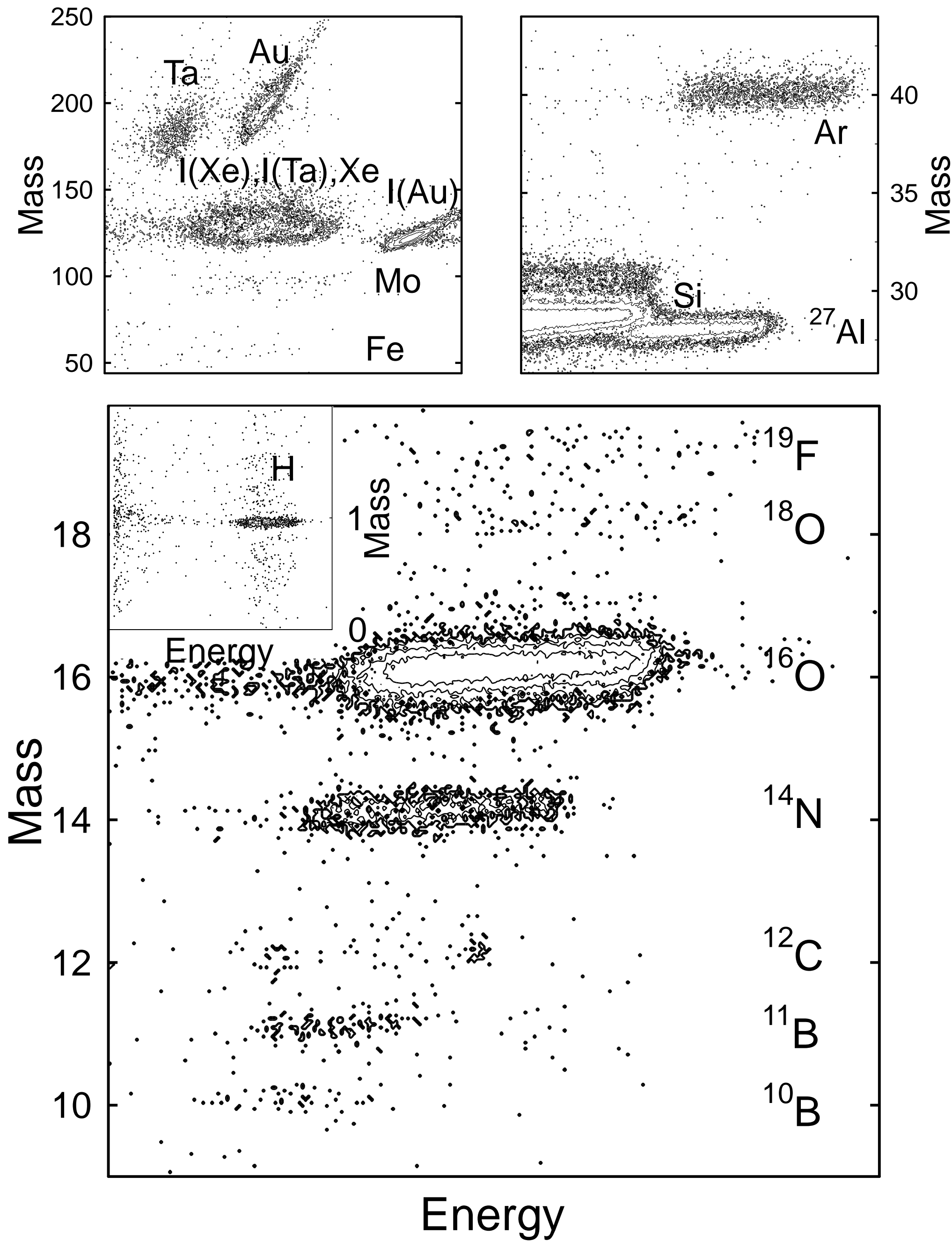

Figure 15: Energy *vs*. mass histograms with different mass ranges from Ta/$Al_xN_yO_z$/Au thin films grown on a silicon wafer measured with 53 MeV $^{127}I^{10+}$ ions using a 15°+25° geometry. The films were grown using magnetron sputtering; they were part of a Round Robin experiment of several ion beam analysis laboratories [91]. Signals from different elements can well be separated except overlapping Xe recoil atom and scattered ^{127}I signals. For instance, the concentration of Mo in the $Al_xN_yO_z$ film was determined to be 0.09±0.02 at.%.

6.3.3 Calculation of concentration distributions

The basic idea in the most common methods for obtaining depth profiles is the backward calculation of the recoiling depth. In the energy spectrum a channel corresponds to a certain depth slice. The depth is calculated using scattering kinematics and either experimental or more often semi-empirical stopping powers [36]. The yield at different depths is then normalised using stopping powers and scattering cross-sections for a given incident ion and sample atoms. If all the sample elements can be analysed, the final depth profiles can be normalised to unity and atomic ratios are obtained. If the film thickness is determined with other methods (*e.g.* optical measurements for transparent films), ERDA is used only for compositional analysis and the stopping power uncertainties for the projectiles become insignificant as the projectile energy loss is the same for all the recoils scattered at the same depth. The relative projectile energy loss when going in and the recoil energy loss when coming out are roughly equal for most projectile-recoil pairs. The density used in the analysis is only a coefficient in the depth scale; it does not influence the concentrations.

A more sophisticated, but also more complicated, way to analyse HI-ERD energy spectra is to use simulation program which produces energy spectra and then compares the experimental and simulated spectra with each other [92, 93]. The final depth profiles of elements are obtained from the simulated depth distributions giving the best fit with the experimental ones. The advantage of this approach is the possibility to add the energy spreading factors like measurement geometry, beam divergence and energy deviation, detector resolution, and energy straggling to the program. In principle, the result should give the true sample structure. However, in HI-ERDA multiple and plural scattering effects are strong, and cannot yet be fully reproduced with the analytical approach [II]. These effects require full MC simulations, which still demand a great deal of computing time. For the analysis of RBS spectra, the programs based on analytical functions are very useful, whereas more complex HI-ERD is still a problem. The Bayesian probability theory [94] in the deconvolution of the measured spectra along with the MC program written in the Accelerator Laboratory is aimed at reproducing the concentration profiles of different elements directly [95].

Many times the final result obtained by means of HI-ERD analysis combines both stopping power dependent and independent analysis. For instance, the ratio of the main constituents (like in oxides) can be obtained very accurately using the stopping power independent approach but the light impurity amounts as well as their locations are determined from the concentration distributions to avoid errors generated by surface and interface peaks. Depth profiles are also used to verify the homogeneity of a thin film. In the present study an analysing program by Arai *et al.* [96] was modified to make it possible to use also the forward scattered projectiles in the analysis.

6.3.4 TOF-ERDA performance

The background and reasonable measuring times normally confine the quantification limit in our TOF-ERDA to a level of 0.05–0.5 at.%, depending on detected element, film thickness, matrix, incident beam, and substrate. Normally the measurement background is the limiting factor in the determination of the quantification limit. Many factors have an influence to the quantification limit in TOF-ERDA and therefore it is very difficult to report specific limits for different elements. If the number of the background events is small, lower quantification levels can be achieved. For instance, in Ref. 8 for 100 nm thick TiO_2 films the lowest residual iodine content in the sample was determined to be 1×10^{14} at./cm^2, which is below the normal quantification limit (0.1 at.%). The result was obtained with roughly 10^{12} incident ^{197}Au ions and the iodine was situated in a totally background-free area of the spectrum.

The mass resolution is often a critical factor, which favours the use of lighter incident ions giving more energy to the relatively light recoils. For the standard 53 MeV ^{127}I ions, mass resolutions are 0.17 u, 0.7 u, 2 u, and 5 u (full width at half maximum) for ^{7}Li, ^{27}Al, ^{59}Co, and ^{93}Nb, respectively, at the surface.

In a normal measurement, sufficient statistics for analysis purposes are collected within 5–90 minutes using 53 MeV ^{127}I ions and beam current of 0.1–0.3 particle-nA. As an example, one 36 minutes long TOF-ERDA measurement of roughly 330 nm thick ALD-grown Sc_2O_3 film [12] resulted in 26353 Sc, 31265 O, and 185 F detected recoils corresponding to concentrations of 39.9±0.5 at.%, 59.7±0.5 at.%, and 0.38±0.03 at.%, respectively. 53 MeV ^{127}I ions were used as incident ions, the irradiation fluence was $\sim 5\times10^{12}$ at./cm^2, and the concentrations were calculated stopping power independently. For another sample, the film thinness or ion beam induced desorption, for instance, can result in much higher inaccuracies in the final results.

Based on the depth resolution (of the order of 10 nm at the surface), and ion beam induced damage, the TOF-ERDA setup in the Accelerator Laboratory is particularly suitable for the analysis of films, which are insensitive to ion beam irradiation and have thicknesses of a few hundred nanometres. The maximum analysis depth is of the order of one micrometre in silicon and $LiNbO_3$ [34].

6.4 Multiple and plural scattering

During its traverse in material, an energetic ion undergoes numerous small angle collisions with the sample atoms. This multiple scattering causes angular spread, which can be described with analytical functions [97–99]. As a result of the small angle scatterings, the almost parallel directions of ions in a beam spread and the original unambiguous measurement geometry is no longer valid in the interpretation of the energy spectra. The scattering angle is only an average value in the recoil energy and scattering cross-section Eqs. (1) and (5). For the simulation of RBS data, MC programs have been introduced [100] but for the simulation of more complicated HI-ERDA, no

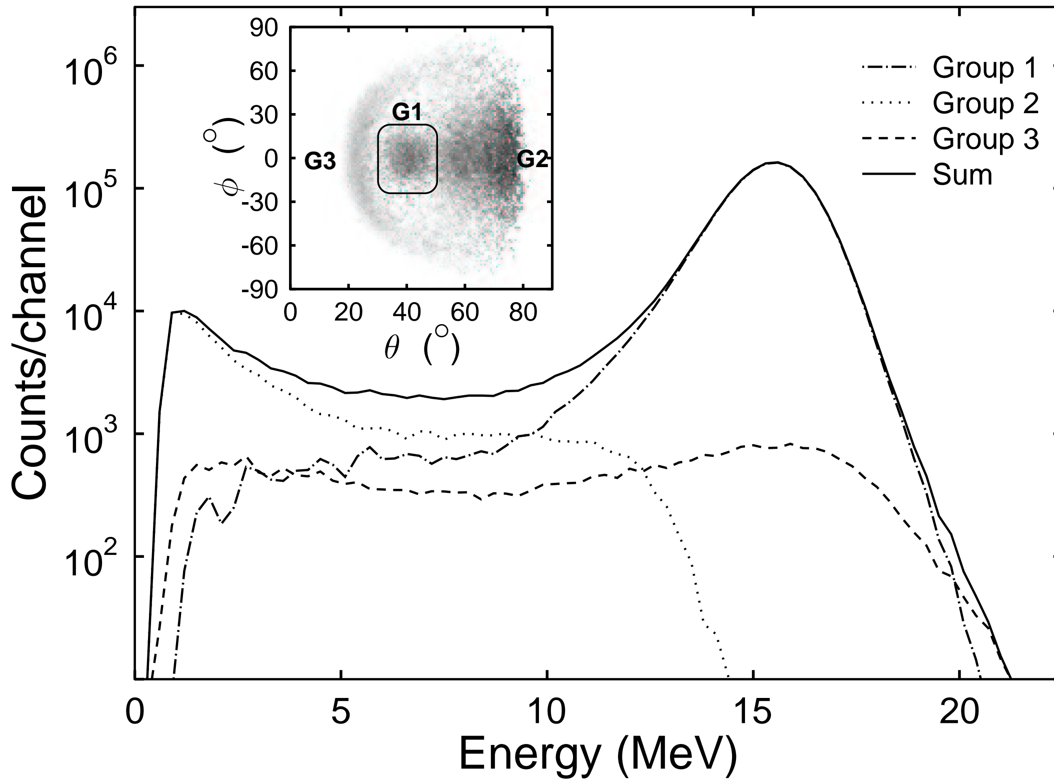

Figure 16: Simulated energy spectra for recoils emitted from deeper Cu layer to three different direction regions from a sample structure of 23 nm Cu/200 nm Ti/23 nm Cu/Si wafer [II]. 53 MeV ^{127}I incident ions were used. The TOF–E detector is located at θ=40°. The selected areas are illustrated in the inset.

MC simulation program like the one utilised for this thesis [II] has been previously used in the literature.

Equally important in the analysis are events where the scattering occurs closer to the sample atom nucleus resulting in a large angle scattering. Although these events are scarce, they can play an important role in the analysis. These scatterings are referred as plural scattering. Due to the nature of these events, no analytical function has been used to simulate them and they require full MC simulations. Despite the exponential development in computer performance, these simulations are not yet achievable within reasonable computing time without major enhancements in the code [101, 102]. By means of the following enhancements in our code [II], the computing performance was improved drastically:

(i) The scattering process and the recoil generation process were treated as separated processes, and the recoil producing cross-section was increased so that each primary ion produces 10 recoils on an average.

(ii) A restricted depth dependent emission solid angle was used for recoils. It was determined by a presimulation procedure.

(iii) A variable depth dependent cross-section was used to produce a roughly equal number of recoils for all depths. Cross-section changes were compensated by the use of statistical weights for recoils.
(iv) A virtual detector having the size of 100 times that of the original detector was used. Recoils hitting the virtual detector were directed to the real detector by recalculating their recoil energy, scattering cross-section, and energy losses.

The basic idea behind our multiple scattering code development [II] was that the simulations should be fast enough to produce energy spectra that can later be utilised in an analysis procedure using the Bayesian probability theory [95].

In the first phase [II] the program was tested with known sandwich sample structures and the recoil emission angle dependency for the detected ions was studied. The program was found to reproduce the measured experimental spectra very well. Before the completion of a new analysis procedure, the current one is a very useful aid in the interpretation of TOF-ERDA results and in the future development of the spectrometer.

The MC program can be used when the original depths and recoiling histories of events in the different parts of the energy spectrum is studied as illustrated in Fig. 16. It was observed that a clear initial recoil direction dependency for deep lying layers in the sample exists for different regions in the energy spectrum. The great majority of the events are emitted close to the detector direction (group 1) whereas the low energy tail is due to the recoils emitted to large angles (θ=60–80°) having a high scattering cross-section but low energies (group 2). The recoils emitted to smaller angles (group 3) are not favoured by the scattering cross-section, but they result in a flat distribution starting from the highest energies and lasting to the lowest ones. If the incident ion scatters close to the surface direction, the effective thickness of the layer increases and detected recoils are emitted towards small angles as in group 3.

The multiple scattering is also an important factor in the TOF-E telescope as the ions scatter in the carbon foils of the TOF detector. As a result they may scatter outside the detector solid angle which is limited by the metal frame carrying the second carbon foil. This effect can be simulated with our MC program. The detection efficiency for different carbon foil thicknesses in T_1 is plotted as a function of the atomic number of recoils in Fig. 17a. In Fig. 17b the detection efficiency of the TOF-E telescope for Nb in $LiNbO_3$ is plotted as a function of the recoiling depth for a 5 $\mu g/cm^2$ carbon foil thickness. In both simulations incident 58 MeV ^{127}I ions and a detector angle of 40° were used. In Fig. 17c the obtained efficiency was used to normalise the depth profile of Nb in a proton exchanged $LiNbO_3$ sample. The original Nb depth profile is presented together with the corrected one, H, and Li depth profiles. For clarity reasons oxygen depth profile at concentration of 60 at.% is not presented. The sample was similar to those studied in [34] and the TOF-E data of the same measurement is presented in Fig. 6.

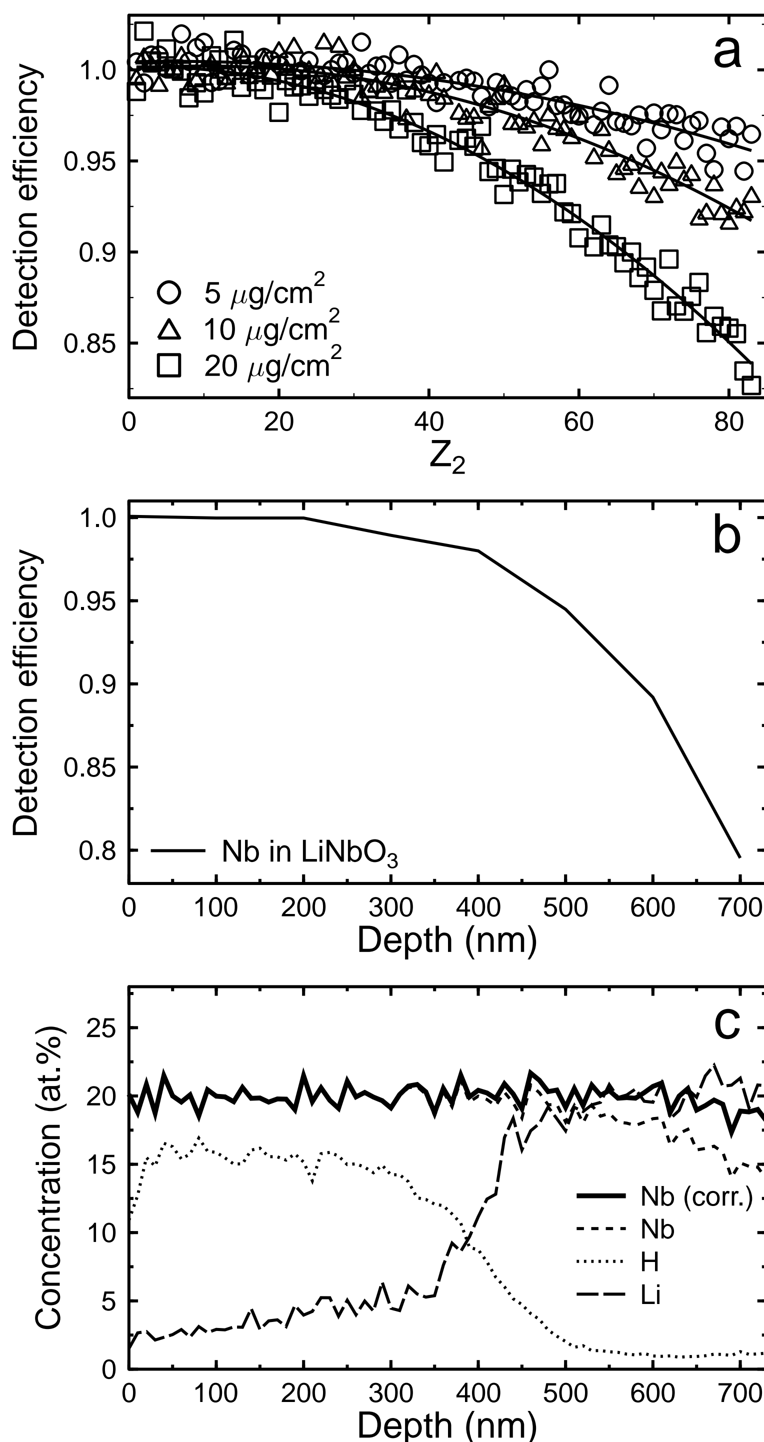

Figure 17: In (a) the detection efficiency of the TOF-E telescope is plotted for 5–20 μg/cm^2 T_1 carbon foil thicknesses in the first timing gate as a function of the recoil atomic number. In (b) the detection efficiency for Nb in $LiNbO_3$ is plotted as a function of the recoil depth using 5 μg/cm^2 carbon foil in the first timing gate. Both results were obtained from MC simulations and the incident ions were 58 MeV ^{127}I ions. In (c) the depth profiles of Nb, H, and Li are plotted for a proton-exchanged $LiNbO_3$ sample and the correction for Nb detection efficiency is used.

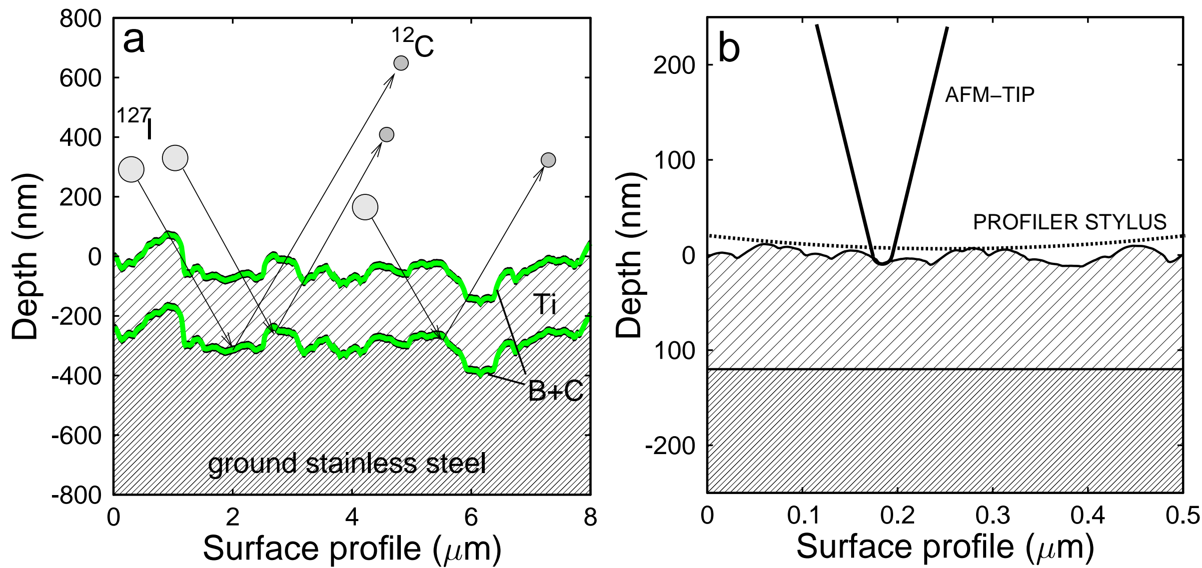

Figure 18: Two different roughness types for thin films. In (a) a film stack of 20 nm B+C/ 220 nm Ti/20 nm B+C on ground (2000 grit paper) stainless steel substrate is shown. In (b) 120 nm ZnS/glass surface profile measured with AFM is shown. In (a) the arrows illustrate the different path lengths in the rough, AFM-measured sample. Because of the different scales in the x- and y-axis of (a), an angle correction was made for in-going incident ions and out-coming recoils, corresponding to a 20°+20° geometry. In (b) a typical AFM tip with a tip curvature radius of 10 nm is plotted along with a profiler stylus having a curvature radius of 2.5 μm.

6.5 Surface roughness

In the analysis of ion beam measurements, the sample surfaces are usually assumed to be smooth. Most analysing programs do not take possible surface or interface roughnesses into account in any way. In reality the samples contain roughnesses and surface structures that should be considered. In the case of thin films the roughnesses can be divided into two main categories: (i) surface roughness of a rough thin film on a flat substrate, and (ii) surface roughness of a thin film with uniform thickness arising from a rough substrate. The first type is common when a well polished semiconductor, glass, and ceramic wafers are used as substrates. The second category is typical for metal substrates and for substrates that have deliberately been left rough for better film adhesion. The two types are illustrated in Fig. 18. The need for a proper surface characterisation in an ion beam analysis becomes evident. For surface characterisation in detail, AFM or STM with a high aspect ratio tip is required. The use of a profiler having a stylus curvature radius in the range of micrometres does not reveal the nanometre-scale surface details (Fig. 18b).

AFM results are often given only as root-mean-square values (rms). These values are then used to depict a certain sample. If all the samples in the study have identical grain sizes and are also uniform in other ways, this approach is defensible. However, in most cases this is not enough: the reader of the publication cannot reproduce the surface by means of an rms value alone. The two situations

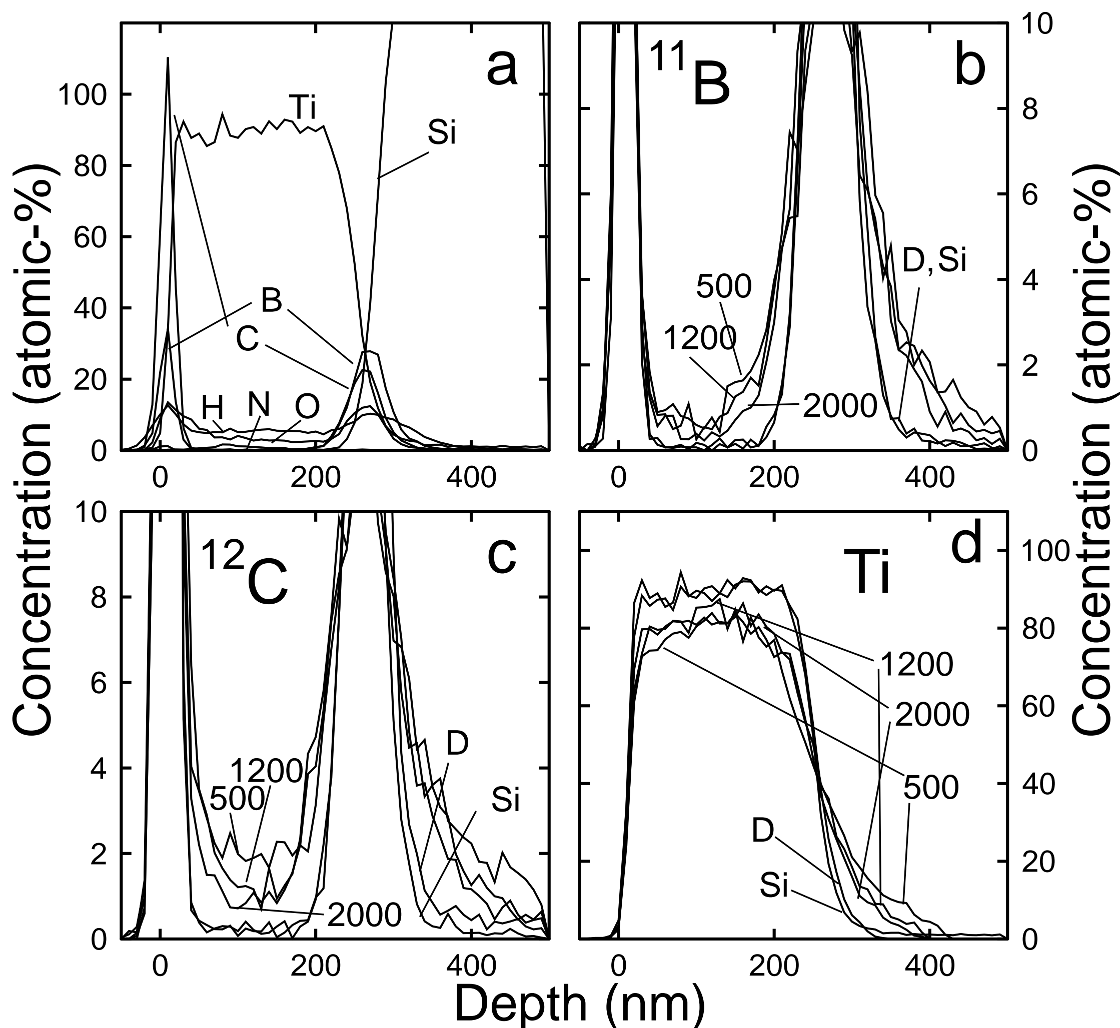

Figure 19: (a) Atomic concentrations of elements in the evaporated layers of a structure B+C(20 nm thick)/Ti(220 nm)/B+C(20 nm) on a silicon substrate. The density used in the depth calculation was the Ti bulk density (4.5 g/cm^3) and therefore less dense layers are seen to be narrower and higher than what they are in reality. (b), (c), and (d) show depth profiles of ^{11}B, ^{12}C, and Ti with different surface roughnesses, ground with sand papers having 500, 1200, and 2000 grits, respectively. The non-broadened ones are from diamond paste polished (D) and flat silicon (Si) samples.

in Fig. 18 are the two extremes. In reality substrates are never totally flat, and the film growth is very rarely exactly uniform. A thin film may also contain hidden voids, or the density can differ in depth due to columnar crystal growth. Even more difficult to analyse is a sample, in which the surface layer is not continuous but consists of individual grains. This kind of surface can be formed during thin film growth or annealing treatments. For this type of film reliable depth profiling is very difficult. The surface characterisations are of great importance especially in diffusion [29, 30, 33] and interface mixing studies, where roughness effects can lead to wrong conclusions.

The experimental and analysis aspects for RBS measurements of rough surfaces have been studied earlier in the Accelerator Laboratory [103] and by other groups [104–106]. Compared to ERDA, the situation for RBS is less difficult when ample surface is (close to) perpendicular to the incident

and backscattered ions. Thus a roughness of type (ii) is invisible in the RBS analysis. However, a roughness of type (i) broadens the low energy edge of the concentration distribution originating from collisions with thin film atoms.

Also for ERDA, some previous studies have been made in which periodic roughness effects have been studied [107]. The roughness has also been approached through projectile and recoil effective path lengths [108, 109], and the influence of the surface roughness on measured depth profiles and implanted ion amounts has been examined [105].

In paper III the substrate roughness was varied by using different grit sand papers in the grinding process. Thin film stacks were evaporated on rough surfaces in the same vacuum. This structure was chosen to mimic the situation in which a sensitive thin film is enclosed between protecting layers and the impurity amounts in the sensitive layer should be studied. This situation occurs for instance with easily oxidising SrS electroluminescent thin films, which should be covered with a protecting Al_2O_3 layer [IV]. The film structure was B+C(20 nm thick)/Ti(220 nm)/B+C(20 nm) on a silicon wafer and the stainless steel substrates. The stainless steel substrates were ground with sand papers having grits 500, 1200, and 2000. In addition, one stainless steel substrate was polished to be mirror-like with diamond paste. A silicon wafer was used as a flat reference.

The depth profiles from measurements performed using 53 MeV ^{127}I beams are presented in Fig. 19. In (a) the depth profiles of all the film elements on a flat silicon substrate are plotted. In (b) and (c) the depth profiles show an increase in the ^{11}B and ^{12}C contents in the Ti layer as a function of the surface roughness. The observed increase is not real but due to the substrate roughness. The ^{11}B and ^{12}C counts inside the Ti films indicate to 4 and 10 times greater impurity concentrations for the grits 2000 and 500, respectively, than what is seen for the films grown on silicon or steel substrates polished with a diamond paste. The detected recoil intensities of ^{11}B and ^{12}C calculated from all the depth profiles were within 5% each others. Another surface roughness related effect can be seen in Fig. 19d. The lowering of the near surface area in the depth profiles obtained from rough samples is due to the reduced probability of such recoils that are produced near the surface and hit the detector without passing any roughness edges.

In paper III an MC simulation was performed for the sample ground with 500 grit paper. The surface topography used in the simulation was obtained from several AFM measurements of the sample. However, the measured energy spectrum was only qualitatively reproduced. The reason for this could be insufficient amount of AFM images to describe all surface characteristics from the TOF-ERDA beam spot area.

The concentration distributions presented in Fig. 19 show that the distributions obtained from ground samples differ significantly from the ones obtained from polished steel or silicon wafer. However, in a visual inspection the sample ground with a 2000 grit paper was a mirror-like and did not deviate from the smooth ones in this sense. The requirement of careful surface characterisation is evident in this case.

6.6 Ion beam induced modification

The most common ion beam analysis methods (RBS, ERDA, NRA) are non-destructive in many applications and do not modify the studied sample significantly. Especially compared to other common depth profiling methods, such as SIMS, XPS, and Auger-electron spectroscopy, in which ion beams are used to erode the sample and a visible crater is formed, these high energy ion beam methods are non-destructive. In the measurements performed in backscattering geometry, detectors with large solid angles can be utilised, because then scattering kinematics do not significantly affect the energy resolution. However, the use of high energy heavy ions and detectors with small solid angles increase the deposited energy per detected particle and, for HI-ERDA, ion beam induced effects should always be taken into consideration. The origin of the modification is in the electronic and nuclear energy loss processes.

Polymer films are an example of a sensitive sample type. Even at low irradiation fluences with heavy ions, a rapid polymer chain braking occurs and the film is destroyed. Different ion induced effects appear in different sample types, and all of these should be taken into account and their influence minimised. On the other hand, we have observed by means of Raman spectroscopy ion beam induced recovery of a degraded structure in annealed diamond-like carbon films with high Si content (33 at.%) [31].

6.6.1 Sputtering and elemental losses

In the analysis of metals and most semiconductors, sputtering can be regarded to be dependent on the nuclear stopping [110]. For typical fluences of the order of 10^{12}–10^{14} ions/cm^2 in TOF-ERDA measurements an exceptionally high sputtering yield of 10 atoms/ion would result in a loss of only one monolayer ($\sim 10^{15}$ at./cm^2) [110]. In comparison with the depth resolution (about 10 nm at the surface) this is a negligible effect. If the analysed layer is very thin, the sputtering may still become a factor limiting accuracy. The sputtering of an analysed layer can be avoided with a protective layer (*i.e.* evaporated gold).

Ion beam induced desorption modifies samples much more than sputtering caused by the nuclear collisions. A typical desorption behaviour is described by an exponential law and the desorption yield decreases and even vanishes with high fluences. Behrisch *et al.* [111] explain this as a result of gradual destruction due to the damage created by incident ions forming a cylinder of a destructed volume around the ion trajectory. For an approximated rectangular shaped cross section of a beam spot, the drop of concentration is exponential at first and the concentration reaches a saturation value rapidly, but for a Gaussian shaped cross section of a beam spot, the elemental concentration losses occur more slowly and linearly. The loss of material is usually limited to volatile species in addition to surface sputtering.

Walker *et al.* [112] studied the elemental losses in insulating materials using 1.1 MeV/nucleon

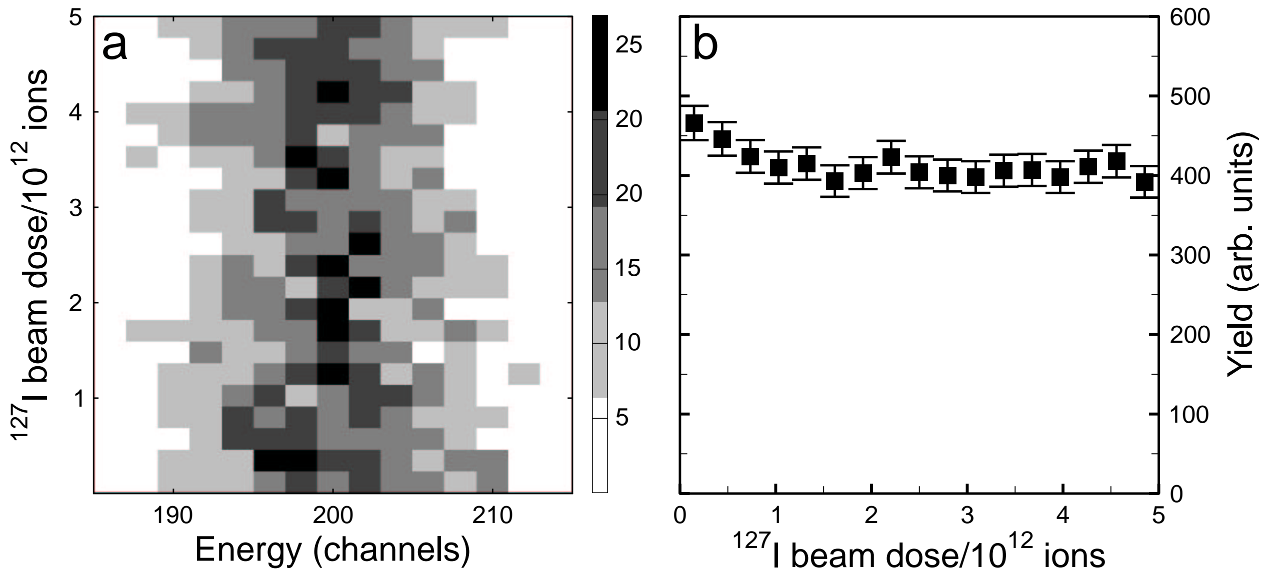

Figure 20: Irradiation fluence *vs*. energy histogram for a silicon wafer sample implanted with 6 keV H and measured with 53 MeV $^{127}I^{10+}$ ions, (a) [85]. The surface hydrogen peak is located at the channel 210. A 10% hydrogen loss can be seen in (b) where the total hydrogen amount is plotted as a function of the irradiation fluence. The beam spot size was about 10 mm^2 and current 200 particle-nA.

^{79}Br, ^{127}I, ^{197}Au, and ^{209}Bi ions. Only negligible losses were found with ceramic targets (Nb_2O_5 and UO_2), but silicon oxynitride and organic materials exhibited observable losses of hydrogen, nitrogen, oxygen and carbon. The losses were smaller for the two heaviest ions when the same statistics were collected. Therefore the use of heavier ions was recommended for sensitive materials. In another study of H and N losses in silicon oxynitride and silicon nitride films during ion irradiation with 1.1 MeV/nucleon ^{79}Br, ^{127}I, and ^{209}Bi ions the damage per detected recoil was observed to be quite equal for different incident ions [113]. Quite contrary results to the previous ones are reported by Timmers *et al*. [114] for silicon nitride films. They observe a large N loss during the analysis of N rich films with 113 and 200 MeV ^{197}Au ions, whereas for 35 MeV ^{35}Cl ions the depletion is negligible. They recommend the use of lighter incident ions in the stoichiometric analysis of SiN films. In all three studies the films were deposited with plasma enhanced chemical vapour deposition method.

Behrisch *et al*. [115] studied ion beam induced deuterium loss for amorphous deutereuted carbon (a-C:D) films with 35 MeV ^{35}Cl, 80 MeV ^{197}Au, and 210 MeV ^{127}I ions. Ion beam induced deuterium desorption was found to be highest for ^{35}Cl ions ($\sim$90% ^{2}D lost) and ^{127}I ions ($\sim$85% ^{2}D lost) but minor for ^{197}Au ions ($\sim$10% ^{2}D lost). The same amount of statistics was collected. In [116] Behrish *et al*. measured a higher desorption rate per incident ion for 200 MeV ^{127}I ions than for 130 MeV ^{58}Ni ions, but the difference in the scattering cross-section results in a better sensitivity by a factor of 2.8 for ^{127}I ions.

In the Accelerator Laboratory, TOF-ERD measurements are done event by event, and the elemental losses during the measurements are always monitored. Therefore the amount of an element can be extrapolated to the beginning of a measurement. An example of hydrogen loss is shown in Fig. 20. The hydrogen energy spectra of the samples used in the Round Robin experiment [85] are plotted to a histogram as a function of the ion fluence in (a) and the total hydrogen yield is plotted as a function of the ion fluence in (b). About half of the total 10% loss during the measurement was regarded to be due to the surface hydrogen loss. In the analysis of ALD grown thin films the desorption of the volatile residual impurities (mainly H) was in some measurements so great that it had an effect on the accuracy of the results reported in paper V and in Refs. 10, 14. The behaviour can be explaned by a three step process [117]: activation, diffusion to the surface mainly through the grain boundaries, and release from the surface as a molecule. In porous materials like the fusion reactor wall materials the desorption can occur even at the depth of several hundred nanometres [118].

Ion induced desorption and surface modification were studied for 43 MeV ^{35}Cl, 48 MeV ^{79}Br, 53 MeV ^{127}I, and 53 MeV ^{197}Au ions and TiN, TaN, and Al_2O_3 films (see Table 3). Some desorption of impurities was observed, but the highest losses ($\sim$20%) were found for hydrogen in Al_2O_3 measured with ^{35}Cl and ^{197}Au. It was not possible to draw any general conclusions concerning the optimal incident ion with respect to the induced desorption for these thin films. In the AFM and STM studies some minor surface modification was observed only for TaN irradiated with ^{79}Br ions. For sensitive samples the beam intensity per unit area should be minimised or detector solid angle increased and damage thereby reduced.

6.6.2 Destruction of the crystalline structure

In semiconductors bombarded with high energy heavy ions, nuclear collisions displace atoms from their lattice sites and generate defects and defect clusters. Walker *et al*. [119] studied this process for Si and GaAs bombarded with 54–98 MeV ^{127}I ions incident at an angle of 22.5° to the target surface. As a result, a measurable but relative small sample damage was observed for a fluence of 10^{14} ions/cm^2. Irradiation induced damage was studied with channelling-RBS and transmission electron microscopy. In HI-ERDA, ion beam induced damage can be measured *in situ* by means of a position sensitive detector and blocking method [120]. In semiconductor materials, this defect generation process was utilised by us for making faster laser optic devices by generating recombination centres to semiconductor saturable-absorber mirrors by a 30 MeV Ni irradiation to a fluence of 10^{12} at./cm^2 [121, 122].

For insulating crystalline materials, amorphisation is much more rapid and strongly related also to the electronic stopping of heavy ions at MeV energies [123, 124]. We observed a rapid amorphisation of α-quartz [125] and $LiNbO_3$ [126] during TOF-ERDA measurements, determined afterwards by means of channelling-RBS and X-ray diffraction, respectively. It is notable, that in both studies no elemental losses were observed even though the crystalline structure was destroyed to a depth of 2 μm.

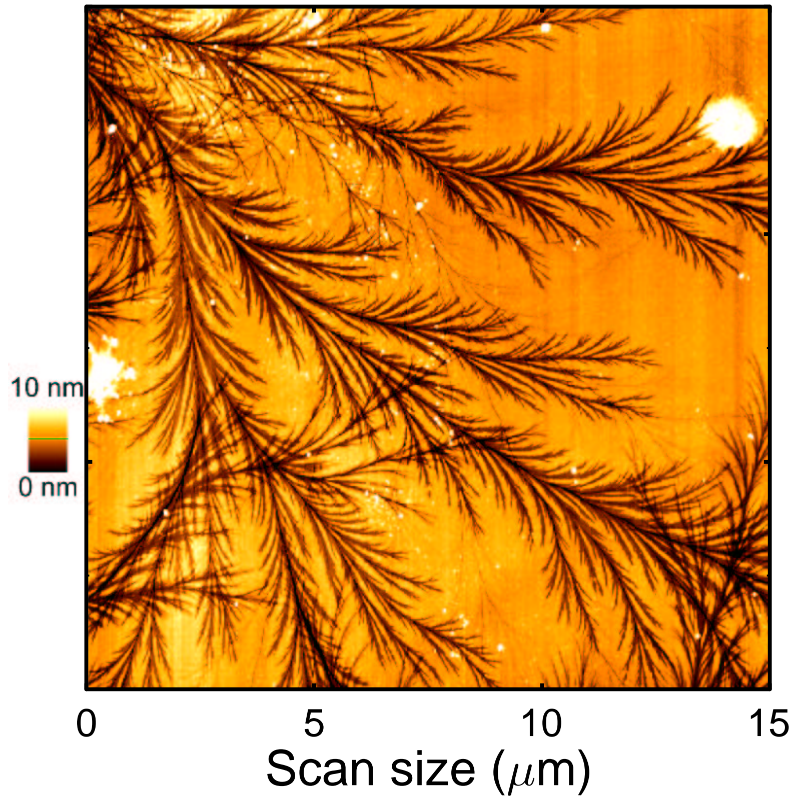

Figure 21: AFM image of high electric current induced dendritic structures in an unimplanted area of an α-quartz sample implanted with 250 keV Ba^+ and annealed in air at 1100°C. The implanted area starting close to upper edge of the image is not shown.

A special type of damage induced by charged ion beams in insulating materials is illustrated in Fig. 21. The figure presents an AFM image of an unirradiated part of an α-quartz sample which was implanted with 250 keV Ba^+ ions at a liquid nitrogen temperature to a fluence of 3.5×10^{16} ions/cm^2 and annealed in air at temperatures up to 1000°C [127]. The unirradiated area was covered with a thin aluminium foil. The dendritic structures in the AFM image are traces of electric sparks which occurred during the implantation. The traces can be observed only quite close to the border between the implanted and unimplanted areas and these structures lead to the implanted area. As these traces became visible after annealing at temperatures over 1000°C, a reason for them could be an amorphisation induced by a high electron current. The electrons are emitted from the covering aluminium foil and migrate towards positively charged irradiated area. High temperature annealing reveal these areas by removing the amorphous silica surrounded by crystalline quartz. Due to ion beam induced modification, these structures can not be observed in the implanted area.

6.7 Summary of TOF-ERDA results

In the research for this thesis TOF-ERDA has been utilised mainly in the analysis of main constituents and impurities in thin films. The thin films to be analysed were deposited using different methods and the impurities detected can in most cases be understood from the growth parameters and precursors used. The main sample and analysis characteristics are summarised in Table 4.

For the multiple scattering and surface roughness studies, tailored thin film structures were grown by electron beam evaporation in papers II and III. The results of these studies are presented in sections 6.4 and 6.5.

Films grown by ALD have been studied in papers IV and VII, and in Refs. 7–24. ALD is based on the saturation of individual, sequentially performed surface reactions between the substrate and the reactants used [1, 128]. When the monolayer is filled, the surface becomes passive for that particular reactant. During the growth, precursors are transported to the reactor by an inert gas (usually N_2) flow. Several precursors can be utilised, depending on the grown material. Between the growth pulses the reactor is purged with an inert gas pulse. For certain precursors, growth temperature, pulse lengths, and thin film substrate can be varied in order to find the optimal growth conditions. The ALD films are normally polycrystalline or amorphous, and they have an excellent step coverage.

At some temperature and pulse length range of the ALD process the chemical reaction proceeds until saturation and the following purge pulse blows the precursor residuals away. However, at lower temperatures the chemical reaction does not necessarily become complete and organic or inorganic residuals are left at the surface, and during the next growth pulse they are covered by the next layer. At too high temperatures the precursors may decompose before reaching the surface or react with wrong species, and again residual impurities can be observed. In TOF-ERD analysis the film main component as well as impurity concentration distributions were obtained. As emerges from Table 4, the incident ions have to be chosen so that elements which are of interest can be detected as well as possible. For example, ^{79}Br ions were utilised in the analysis if iodide precursors were used during the film growth. In most cases some negligible hydrogen and carbon losses from surface were observed during the ion beam irradiation. If the losses were significant, the original content was extrapolated from data collected event by event. Especially for the processes in which organic precursors were used, the ability of an accurate H and C analysis was proven to be very useful.

The analysis results of $Cu_xIn_ySe_z$ films grown by electrodeposition [VI] are presented in Fig. 11 and Table 2. Although the film surfaces were even visually rough and H losses were observed during the measurements, TOF-ERD analysis gave important information of the light impurity elements. In the analysis of main components, TOF-ERDA results agreed well with RBS results.

Ion beam assisted deposition was applied for the growth of hard coatings [25, 26] and reactive magnetron for FeN films. TOF-ERD analysis provided information on the film uniformity and the

impurity contents.

Deuterium diffusion behaviour and concentration distributions were determined for pulsed vacuum arc deposition grown films [V, 29–31]. Diamond-like carbon films were doped with different silicon contents. TOF-ERDA results for deuterium were used to normalise SIMS depth profiles. In Ref. 28 diamond-like carbon films with hydrogen reservoirs were studied with TOF-ERDA. Different hydrogen doping methods were studied and the hydrogen concentrations were provided by TOF-ERDA.

TOF-ERDA has been found to be a useful tool in migration studies. The oxygen activated recrystallisation and out-migration of the implanted Li-ions in α-quartz has been studied earlier in our laboratory [129]. In this thesis the ^{18}O in-migration and Na out-migration was studied [33]. The migration of elements was studied with TOF-ERDA and the recrystallisation with channelling-RBS. In paper VII ^{18}O and ^{37}Cl ions were coimplanted with ^{63}Cu ions to study the photoluminescence (PL) colour and intensity, and the migration behaviour as a function of the fluence and post-implantation annealing temperature. The migration behaviour was studied with TOF-ERDA.

Table 4: Summary of TOF-ERD analysis.

Material	Precursors[1] and induced modifications	Detected elements	Incident ions	Other methods[2]	Comments	Ref.
ALD-grown oxides						
Al_2O_3, Ta_2O_5	$Al(CH_3)_3$, $Ta(OEt)_5$, H_2O	Ta,Al,O,C,H	34 MeV ^{127}I	XRD[3]	early study	[7]
TiO_2	TiI_4, H_2O_2	Ti,O,H,I	48 MeV ^{197}Au	XRD	low I levels (1–15$\times10^{14}$ at./cm^2)	[8]
(Al,Zr,Hf,Ta,Si) oxides	metal alkoxides and halides	Ta,Hf,Zr,Ti,Cl,Si,O,C,H	53 MeV ^{127}I			[9]
MgO	cp_2Mg, H_2O	Mg,O,C,H	53 MeV ^{127}I	XRD,XPS[4]	Ion beam induced H loss	[10]
Y_2O_3	$Y(thd)_3$,$Y(thd)_3$(biby),$Y(thd)_3$(phen),O_3	Y,F,O,N,C,H	53 MeV ^{127}I	XRD,FTIR,XPS		[11]
Sc_2O_3	$Sc(thd)_3$, $(cp_3)Sc$,H_2O,H_2O_2,O_3	Sc,O,H,C,F	53 MeV ^{127}I	XRD,FTIR[5]		[12]
$Y_xZr_yO_z$	$Y(thd)_3$,$Zr(thd)_4$,cp_2ZrCl_2,$cp_2Zr(CH_3)_2$,O_3	Y,Zr,O,H,C,F,Cl	53 MeV ^{127}I	XRD,XRF[6],SEM-EDX[7]		[13]
$Zr_xAl_yNb_zO_s$,$Zr_yAl_zO_x$	$Nb(OC_2H_5)_5$, $ZrCl_4$,$Al(CH_3)_3$, H_2O	Nb,Zr,Cl,Al,O,C,H	53 MeV ^{127}I	XRD	Zr and Nb not separated	[14]
HfO_2-Al_2O_3-Nb_2O_5	$HfCl_4$,HfI_4,$Nb(OC_2H_5)_5$,$Al(CH_3)_3$,H_2O	Hf,Nb,Cl,Al,O,C,H	53 MeV ^{127}I	XRD	forw. scatt. ^{127}I used in Hf determ.	[15]
ZrO_2	ZrI_4, H_2O,H_2O_2	I,Zr,O,H	48 MeV ^{197}Au	RHEED[8]	Ion beam induced H loss	[16]
Er_2O_3	$Er(thd)_3$, O_3	Er,O,H,C,F	51 MeV ^{127}I	XRD		[17]
HfO_2	HfI_4,O_2	Hf,I,O,H	48 MeV ^{79}Br	XRD,SEM-EDX	forw. scatt. ^{79}Br used in Hf determ.	[18]
HfO_2	HfI_4,$HfCl_4$,H_2O	Hf,I,Cl,O,H	48 MeV ^{79}Br	XRD	forw. scatt. ^{79}Br used in Hf determ.	[19]
$SrTiO_3$	$Sr(C_5{}^iPr_3H_2)_2$,$Ti(O^iPr)_4$, H_2O	Sr,Ti,Al,O,C,H	34 MeV ^{127}I	RBS,XRD,SEM-EDX		[20]
$LaAlO_3$	$La(thd)_3$,$AlC_5H_8O_2$,O_3	La,Al,F,O,C,H	48 MeV ^{197}Au	RBS,XPS,XRD,FTIR		[21]
ALD-grown nitrides						
TaN	$TaCl_5$,$TaBr_5$,NH_3,$C_4H_{11}N$,C_3H_7N	Ta,Br,Cl,O,N,C,H	53 MeV ^{127}I	XRD,SEM-EDX	forw. scatt. ^{127}I used in Ta determ.	[IV]
TaN	$TaCl_5$,C_3H_9Al	Ta,Cl,Al,O,N,C,H	53 MeV ^{127}I	XRD,SEM-EDX	forw. scatt. ^{127}I used in Ta determ.	[22]
TiN	$TiCl_4$,TiI_4,$^tBuNH_2$,allylNH_2,NH_3	Ti,O,N,C,H	53 MeV ^{127}I and ^{197}Au	XRD		[23]
ALD-grown sulfides						
SrS,BaS	$(C_5{}^iPrH_2)_2Sr(THF)$,$(C_5(CH_3)_5)_2Sr(THF)_x$, $(C_5(CH_3)_5)_2Ba(THF)_x$,H_2S	Ba,Sr,S,O,C,H	34 and 53 MeV ^{127}I	XRD		[24]
Electrodeposition grown films						
$CuInSe_2$	CuCl,SeO_2,$InCl_3$	In,Mo,Se,Cu,K,S,O,N,C,H	48 MeV ^{127}I	RBS,XRD,SEM-EDX	rough films, H loss	[V]
Ion beam assisted deposition grown nitrides						
C_xN_y	evap. C,N_2+Ar	Ar,O,N,C,H	48 MeV ^{127}I	XPS,XANES[9],μ-Raman		[25]
$B_xC_yN_z$	evap. B_4C,N_2+Ar	Ar,O,C,N,B,H	48 MeV ^{127}I	XANES		[26]
Reactive magnetron sputtering grown films						
FeN_y	Fe,N_2,Ar	Fe,O,N,C,H	37 MeV ^{197}Au	RBS,CEMS[10],XRD	early study	[27]
Pulsed vacuum arc deposition grown films						
ta-C[1],H:ta-C,CH:Ti	graphite,H_2,CH_4	Ti,C,H	34 MeV ^{127}I		low friction films with H reserv.	[28]
ta-C_xSi_y:D	graphite,Si,D_2	Si,O,C,D,H	53 MeV ^{127}I	RBS,SIMS,SEM-EDX	ERDA normalized SIMS spectra	[VI], [29–31]
Ion beam modification and migration studies						
(100)GaAs	20 keV Be impl.	As,Ga,Be	37 MeV ^{197}Au	channeling-RBS,SIMS	migration studies	[32]
α-quartz	50 keV Na impl.	Si,Na,^{18}O,^{16}O	53 MeV ^{127}I	channeling-RBS	migration studies	[33]
SrS	60 keV ^{18}O, 80 keV ^{37}Cl, 120 keV ^{63}Cu	Sr,Cu,Cl,S,Al,^{18}O,^{16}O,C,H	34 MeV ^{127}I		migration and PL emission study	[VII]
$LiNbO_3$	proton exchange	Nb,O,Li,H	55 MeV ^{127}I,48 MeV ^{79}Br, 43 MeV ^{35}Cl	XRD	maximum depth of >1 μm was reached in the analysis	[34]
$LiNbO_3$	Zn in-diffusion	Nb,Zn,O,Li	55 MeV ^{127}I	XRD		[35]

[1] thd = $C_{11}H_{19}O_2$, cp = C_5H_5, biby = $C_{10}H_8N_2$, phen = $C_{12}H_8N_2$, ^{i}Pr = i-C_3H_7, tma = C_3H_9Al, ^{t}Bu = $(CH_3)_3C$-, allyl = CH_2=$CHCH_2$-, THF = C_4H_8O, ta-H = tetrahedral amorphous carbon, same as DLC (diamond-like carbon) ; [2] Other compositional characterisation methods used; [3] X-ray diffraction; [4] X-ray photoelectron spectroscopy; [5] Fourier transform infrared spectrometer; [6] X-ray fluorescence; [7] Scanning electron microscopy with energy dispersive X-ray detector; [8] Reflection high-energy electron diffractometry; [9] X-ray absorption near-edge spectroscopy; [10] Conversion electron Mössbauer spectroscopy

7 CONCLUSIONS AND CONSIDERATIONS FOR FUTURE RESEARCH

In the research for this thesis TOF-ERDA measurements have been performed to characterise a wide range of different samples. By means of the method developed for hydrogen detection and by making use of forward scattered incident ions in the analysis, a quantitative, standard-free, and rapid detection method for all sample elements was obtained. Three out of the four main matters influencing the usability of heavy ion ERDA have been studied: understanding of multiple scattering, surface roughness, and ion beam induced damage effects is a key to a correct interpretation of the measured data. The fourth factor, stopping power inaccuracy, can be avoided in many cases by using the total elemental yields and scattering cross-sections in the analysis. Today TOF-ERDA is an analysis method extensively used in the Accelerator Laboratory. It is capable of characterising various sample types with high reliability. The standard operation procedures used in the technical operation and analysis guarantee good day-to-day reproducibility. This has enabled us to use TOF-ERDA also in the analysis of industrial samples.

The driving force behind the present study was the rapid growth of thin film applications and development of film growth methods. Thin film research requires fast and reliable feedback, and it should be possible to analyse new materials without tedious use of standard samples and preliminary knowledge of sample structures and constituents. In this field TOF-ERDA is a very powerful technique. In measurements of, for instance, low impurity levels, diffusion behaviour, and elemental ratios, other methods like RBS and SIMS are complementary to TOF-ERDA.

The further development of the TOF-ERDA method will focus on the position sensitivity of the telescope. This would enable us to enlarge the solid angle of the detector, and at the same time improve the depth resolution at the sample surface by correcting kinematic broadening. In the future we are planning to build a TOF-E telescope in which the position information is obtained from the magnified electron signal of the timing gate. Reduced ion beam induced damage and better depth resolution are mandatory conditions in the depth profiling of gate oxides in their normal thicknesses of a few nanometres.

The versatility of the TOF-ERDA beam line has recently been increased by mounting an X-ray detector to the chamber at angle of 90°. Preliminary measurements have shown the usefulness of the additional detector in the analysis of oxides which contain elements having neighbouring atomic numbers and overlapping isotope masses. By the use of the X-ray detector also those elements that are not separated in TOF-ERDA data can be quantified simultaneously.

ACKNOWLEDGEMENTS

I wish to thank Professor Juhani Keinonen, Head of the Department of Physical Sciences, for giving me the opportunity to work in the field of ion beam physics. I also thank him warmly for his supervision of my work during the preparation of the current thesis.

My thanks are also due to the former and current Heads of the Accelerator Laboratory, Professor Jyrki Räisänen and Dr Eero Rauhala, for placing the facilities of the laboratory at my disposal.

I have had the chance to collaborate with two Finnish research groups which perform thin film research at the highest international level. I want to thank Professor Markku Leskelä and Dr Mikko Ritala, University of Helsinki, and Professor Lauri Niinistö, Helsinki University of Technology, as well as the co-authors of all the papers included in this thesis.

I want to thank Dr Janne Jokinen for tutoring me with the TOF-ERDA basics. For his sharing a room, fits of laughter, and periods of concern with me for a number of years, I want to extend warm thanks to Dr Kai Arstila, who has been such a good friend all of this time.

The working atmosphere at the Laboratory has always been positive and encouraging and it has been understood that it is also of importance to have occacional relaxation in spare time. For both scientific and non-scientific considerations, my special thanks are due to Dr Kai Nordlund, Dr Emppu Salonen, Dr Jura Tarus, Dr Arkady Krasheninnikov, Marcus Gustafsson, M.Sc., and Petteri Pusa, M.Sc. Mr Heikki Sepponen deserves warm thanks for the stable operation of the EGP-10-II accelerator.

During my Helsinki years, the Keskisuomalainen Osakunta nation KSO and all the friends at KSO have played an important role in my life. The time spent at the activities at KSO has served as a stable counterbalance for the research work and vice versa.

I want to thank my parents Paula and Kari and my sister Anu, who have encouraged, supported, and believed in me all the time.

My warmest thanks are due to Katri, who has loved and supported me through an entire decade.

Financial support from the Magnus Ehrnrooth foundation and the Vilho, Kalle, and Yrjö Väisälä foundation is gratefully acknowledged.

Helsinki, September 2002

T. S.

References

[1] T. Suntola and J. Hyvärinen, *Atomic layer epitaxy*, Ann. Rev. Mat. Sci. **15**, 177 (1985).

[2] Intel Corporation, *Intel Announces Breakthrough In Chip Transistor Design*, (26th Nov. 2001, Santa Clara, California).

[3] J. L'Ecuyer, C. Brassard, C. Cardinal, J. Chabbal, L. Deschênes, J. P. Labrie, B. Terreault, J. G. Martel, and R. St.-Jacques, *An accurate and sensitive method for the determination of the depth distribution of light elements in heavy materials*, J. Appl. Phys. **47**, 381 (1976).

[4] G. Binnig, H. Rohrer, C. Gerber, and E. Weibel, *Tunneling through a controllable vacuum gap*, Appl. Phys. Lett. **40**, 178 (1982).

[5] G. Binnig, H. Rohrer, C. Gerber, and E. Weibel, *Surface studies by scanning tunneling microscopy*, Phys. Rev. Lett. **49**, 57 (1982).

[6] G. Binnig, C. Quate, and C. Gerber, *Atomic force microscope*, Phys. Rev. Lett. **56**, 930 (1986).

[7] R. Matero, A. Rahtu, M. Ritala, M. Leskelä, and T. Sajavaara, *Effect of Water Dose on the Atomic Layer Deposition Rate of Oxide Thin Films*, Thin Solid Films **368**, 1 (2000).

[8] K. Kukli, M. Ritala, M. Schuisky, M. Leskelä, T. Sajavaara, J. Keinonen, T. Uustare, and A. Hårsta, *Atomic layer deposition of titanium oxide from TiI_4 and H_2O_2*, Chem. Vap. Dep. **6**, 303 (2000).

[9] M. Ritala, K. Kukli, A. Rahtu, M. Leskelä, T. Sajavaara, and J. Keinonen, *Atomic layer deposition of oxide thin films with a novel chemical approach*, Science **288**, 319 (2000).

[10] M. Putkonen, T. Sajavaara, and L. Niinistö, *Enhanced growth rate in atomic layer epitaxy deposition of magnesium oxide thin films*, J. Mater. Chem. **10**, 1857 (2000).

[11] M. Putkonen, T. Sajavaara, S. Johansson, and L. Niinistö, *Low temperature ALE deposition of Y_2O_3 thin films from β-diketonate precursors*, Chem. Vap. Dep. **7**, 44 (2001).

[12] M. Putkonen, M. Nieminen, J. Niinistö, L. Niinistö, and T. Sajavaara, *Surface-controlled deposition of Sc_2O_3 thin films by atomic layer epitaxy using β-diketonate and organometallic precursors*, Chem. Mater. **13**, 4701 (2001).

[13] M. Putkonen, T. Sajavaara, J. Niinistö, L.-S. Johansson, and L. Niinistö, *Deposition of yttria-stabilized zirconia thin films by atomic layer epitaxy from beta-diketonate and organometallic precursors*, J. Mater. Chem. **12**, 442 (2002).

[14] K. Kukli, M. Ritala, M. Leskelä, T. Sajavaara, J. Keinonen, D. Gilmer, S. Bagchi, and L. Prabhu, *Atomic Layer Deposition of Al_2O_3, ZrO_2, Ta_2O_5 and Nb_2O_5 Based Nanolayered Dielectrics*, Non-cryst. Solids **303**, 35 (2002).

[15] K. Kukli, M. Ritala, M. Leskelä, T. Sajavaara, J. Keinonen, D. Gilmer, R. Hedge, R. Rai, and L. Prabhu, *Atomic Layer Deposition of HfO_2 thin films and nanolayered HfO_2-Al_2O_3-Nb_2O_5 dielectrics*, J. Mater. Sci.: Mat. in Electr., submitted for publication.

[16] K. Kukli, M. Ritala, T. Uustare, J. Aarik, K. Forsgren, T. Sajavaara, M. Leskelä, and A. Hårsta, *Influence of thickness and growth temperature on the properties of zirconium oxide films grown by atomic layer deposition on silicon*, Thin Solid Films **410**, 53 (2002).

[17] J. Päiväsaari, M. Putkonen, T. Sajavaara, and L. Niinistö, *Atomic layer deposition of erbium oxide thin films*, J. Mater. Chem. submitted for publication.

[18] J. Aarik, J. Sundqvist, A. Aidla, J. Liu, T. Sajavaara, K. Kukli, and A. Hårsta, *Hafnium tetraiodide and oxygen as precursors for atomic layer deposition of hafnium oxide thin films*, Thin Solid Films, submitted for publication.

[19] K. Kukli, M. Ritala, T. Sajavaara, J. Keinonen, and M. Leskelä, *Comparison of hafnium oxide films grown by atomic layer deposition from iodide and chloride precursors*, Thin Solid Films, in press.

[20] M. Vehkamäki, T. Hänninen, M. Ritala, M. Leskelä, T. Sajavaara, E. Rauhala, and J. Keinonen, *Atomic layer deposition of $SrTiO_3$ thin films from a novel strontium precursor strontium bis(tri-isopropyl cyclopentadienyl)*, Chem. Vap. Dep. **7**, 75 (2001).

[21] M. Nieminen, T. Sajavaara, E. Rauhala, M. Putkonen, , and L. Niinistö, *Surface controlled growth of $LaAlO_3$ thin films by atomic layer epitaxy*, J. Mater. Chem. **11**, 2340 (2001).

[22] P. Alen, M. Juppo, M. Ritala, T. Sajavaara, J. Keinonen, and M. Leskelä, *Atomic layer deposition of Ta(Al)N(C) thin films using trimethylaluminum as a reducing agent*, J. Electrochem. Soc. **148**, G566 (2001).

[23] M. Juppo, P. Alen, M. Ritala, T. Sajavaara, J. Keinonen, and M. Leskelä, *Atomic layer deposition of titanium nitride thin films using tert-butylamine and allylamine as reductive nitrogen sources*, Electrochem. Solid State Lett. **5**, C4 (2002).

[24] J. Ihanus, T. Hänninen, T. Hatanpää, T. Aaltonen, I. Mutikainen, T. Sajavaara, J. Keinonen, M. Ritala, and M. Leskelä, *Atomic layer deposition of SrS and BaS thin films using cyclopentadienyl precursors*, Chem. Mater. **14**, 1937 (2002).

[25] R. Gago, I. Jiménez, C. Cáceres, F. Agulló-Rueda, T. Sajavaara, J. M. Albella, A. Climent-Font, I. Vergara, J. Räisänen, and E. Rauhala, *Hardening mechanisms in graphitic carbon nitride films grown with N_2/Ar ion assistance*, Chem. Mater. **13**, 129 (2001).

[26] R. Gago, I. Jiménez, T. Sajavaara, E. Rauhala, , and J. Albella, *X-ray absorption studies of cubic boron-carbon-nitrogen films grown by ion beam assisted evaporation*, Diam. Rel. Mat. **10**, 1165 (2001).

[27] L. Rissanen, P. Schaaf, M. Neubauer, K.-P. Lieb, J. Keinonen, and T. Sajavaara, *The production of the new cubic FeN phase by reactive magnetron sputtering*, App. Surf. Sci. **138–139**, 261 (1999).

[28] J. Koskinen, H. Ronkainen, S. Varjus, T. Muukkonen, and T. Sajavaara, *Low friction ta-C films with hydrogen reservoirs*, Diam. Rel. Mat. **10**, 1030 (2001).

[29] E. Vainonen-Ahlgren, T. Sajavaara, W. Rydman, T. Ahlgren, K. Nordlund, and J. Keinonen, *Deuterium retention in Si doped carbon films*, Proceedings of the international workshop on hydrogen retention in fusion materials, ed. C.H. Wu, Kluwer, Dodrecht, the Netherlands, 281 (2000).

[30] J. Likonen, E. Vainonen-Ahlgren, T. Ahlgren, S. Lehto, T. Sajavaara, W. Rydman, J. Keinonen, J. Katainen, and C. Wu, *Annealing Behaviour of Deuterium in Silicon Doped Carbon Films*, Contributions to Plasma Physics **42**, 445 (2002).

[31] L. Khriachthev, E. Vainonen-Ahlgren, T. Sajavaara, T. Ahlgren, and J. Keinonen, *Stability of Si-C films prepared by a pulsed arc discharge method: Thermal treatment and heavy-ion irridation*, J. Appl. Phys. **88**, 2118 (2000).

[32] T. Sajavaara, J. Jokinen, K. Arstila, and J. Keinonen, *TOF-ERDA Spectrometry Applied for the Analysis of Be Migration in (100) GaAs*, Nucl. Instr. and Meth. in Phys. Res. B **139**, 225 (1998).

[33] S. Dhar, S. Gasiorek, M. Lang, K. Lieb, J. Keinonen, and T. Sajavaara, *Epitaxial recrystallization of amorphized α-quartz after sodium ion implantation and oxygen annealing*, Surface and Coatings Technology in press.

[34] O. Espeso-Gil, T. Sajavaara, G. D. L. Paliza, G. García, F. Agulló-López, J. Cabrera, and A. Climent-Font, *Compositional Characterization of Proton-Exchanged Waveguides in $LiNbO_3$ by Heavy Ion Elastic Recoil Detection*, Ferroelectrics, in press.

[35] O. Espeso-Gil, G. García, F. A. López, A. Climent-Font, T. Sajavaara, M. Domenech, E. Cantelar, and G. Lifante, *Characterization of surface layers in Zn diffused $LiNbO_3$ waveguides by heavy ion elastic recoil detection*, Appl. Phys. Lett., in press.

[36] J. Ziegler, J. Biersack, and U. Littmark, *The Stopping and Range of Ions in Solids* (Pergamon Press, Inc., New York, 1985).

[37] W. Brandt and M. Kitagawa, Phys. Rev. B **25**, 5631 (1982).

[38] J. Ziegler and J. Biersack, SRIM-2000 computer code, www.srim.org.

[39] J. Ziegler, *Stopping of energetic light ions in elemental matter*, Appl. Phys. Lett. **85**, 1249 (1999).

[40] K. Arstila, J. Keinonen, and P. Tikkanen, *Stopping power for low-velocity heavy ions: (0.01–0.9) MeV/nucleon Si ions in 18 (Z=13-79) metals*, Nucl. Instr. and Meth. in Phys. Res. B **101**, 321 (1995).

[41] K. Arstila, J. Keinonen, P. Tikkanen, and A. Kuronen, *Stopping power for low-velocity heavy ions: (0–1.0)-MeV/nucleon Mg ions in 17 (Z=22–79) elemental solids*, Phys. Rev. B **41**, 6117 (1990).

[42] K. Arstila, J. Keinonen, P. Tikkanen, and A. Kuronen, *Stopping power for low-velocity Mg ions in Si, Ge, and GaAs*, Phys. Rev. B **43**, 13967 (1991).

[43] J. Keinonen, K. Arstila, and P. Tikkanen, *Electronic stopping power of Si and Ge for MeV-energy Si and P ions*, Appl. Phys. Lett. **60**, 228 (1992).

[44] Y. Zhang, G. Possnert, and H. Whitlow, *Measurements of the mean energy-loss of swift heavy ions in carbon with high precision*, Nucl. Instr. and Meth. in Phys. Res. B **183**, 34 (2001).

[45] Y. Zhang and G. Possnert, *Electronic stopping power of swift heavy ions in carbon*, Nucl. Instr. and Meth. in Phys. Res. B **190**, 69 (2002).

[46] W. Trzaska, T. Alanko, V. Lyapin, and J. Räisänen, *A novel method for obtaining continuous stopping power curves*, Nucl. Instr. and Meth. in Phys. Res. B **183**, 203 (2001).

[47] T. Alanko, W. Trzaska, V. Lyapin, J. Räisänen, G. Tiourine, and A. Virtanen, *Simultaneous wide-range stopping power determination for several ions*, Nucl. Instr. and Meth. in Phys. Res. B **190**, 60 (2002).

[48] W. Chu, *Calculation of energy straggling for protons and helium ions*, Phys. Rev. A **13**, 2057 (1976).

[49] Q. Yang, D. O'Connor, and Z. Wang, *Empirical formulae for energy loss straggling of ions in matter*, Nucl. Instr. and Meth. in Phys. Res. B **61**, 149 (1991).

[50] W. Bragg and R. Kleeman, *On the alpha particles of radium, and their loss of range in passing through various atoms and molecules*, Philos. Mag. **10**, 318 (1905).

[51] K. Arstila, *An experimental method for precise determination of electronic stopping powers for heavy ions*, Nucl. Instr. and Meth. in Phys. Res. B **168**, 473 (2000).

[52] B. Terreault, J. Martel, R. St-Jacques, and J. L'Ecuyer, *Depth profiling of light elements in materials with high-energy ion beams*, J. Vac. Sci. Technol. **14**, 492 (1977).

[53] B. Doyle and P. Peercy, *Technique for profiling ^{1}H with 2.5-MeV Van de Graaff accelerators*, Appl. Phys. Lett. **34**, 811 (1979).

[54] W. Bik, C. de Laat, and F. Habraken, *On the use of a dE-E telescope in elastic recoil detection*, Nucl. Instr. and Meth. in Phys. Res. B **64**, 832 (1992).

[55] F. Habraken, *Light element depth profiling using elastic recoil detection*, Nucl. Instr. and Meth. in Phys. Res. B **68**, 181 (1992).

[56] M. Petrascu, I. Berceanu, I. Brancus, A. Buta, M. Duma, C. Grama, I. Lazar, I. Mihai, M. Petrovici, V. Simion, M. Mihaila, and I. Ghita, *A method for analysis and profiling of boron, carbon and oxygen impurities in semiconductor wafers by recoil atoms in heavy ion beams*, Nucl. Instr. and Meth. in Phys. Res. B **4**, 396 (1984).

[57] L. Seiberling, *Si-H and C-H bond breaking during MeV-ion bombardment of native oxide of silicon*, Nucl. Instr. and Meth. in Phys. Res. B **24/24**, 526 (1987).

[58] R. Behrisch, R. Grötzschel, E. Hentschel, and W. Assmann, *HIERD analysis of the low-Z deposits on probes from the vessel walls of fusion experiments*, Nucl. Instr. and Meth. in Phys. Res. B **68**, 245 (1992).

[59] D. Avasthi, D. Kabiraj, A. Bhagwat, G. Mehta, V. Vankar, and S. Ogale, *Simultaneous detection of light elements by ERDA with gas-ionisation/Si Delta E-E detector telescope*, Nucl. Instr. and Meth. in Phys. Res. B **93**, 480 (1994).

[60] J. Forster, P. Currie, J. Davies, R. Siegele, S. Wallace, and D. Zelenitsky, *Elastic recoil detection (ERD) with extremely heavy ions*, Nucl. Instr. and Meth. in Phys. Res. B **113**, 308 (1996).

[61] C. Gossett, *Use of magnetic spectrometer to profile light elements by elastic recoil detection*, Nucl. Instr. and Meth. in Phys. Res. B **15**, 481 (1986).

[62] R. Groleau, S. Gujrathi, and J. Martin, *Time-of-flight system for profiling recoiled light elements*, Nucl. Instr. and Meth. **218**, 11 (1983).

[63] J. Thomas, M. Fallavier, D. Ramdane, N. Chevarier, and A. Chevarier, *High resolutuion depth profiling of light elements in high atomic mass materials*, Nucl. Instr. and Meth. **218**, 125 (1983).

[64] H. Whitlow, G. Possnert, and C. Petersson, *Quantative mass and energy dispersive elastic recoil spectrometry: Resolution and efficiency considerations*, Nucl. Instr. and Meth. in Phys. Res. B **27**, 448 (1987).

[65] E. Arai, H. Funaki, M. Katayama, and K. Shimizu, *TOF-ERD experiments using a 10 MeV* ^{35}*Cl beam*, Nucl. Instr. and Meth. in Phys. Res. B **64**, 296 (1992).

[66] P. Goppelt, B. Gebauer, D. Fink, M. Wilpert, T. Wilpert, and W. Bohne, Nucl. Instr. and Meth. in Phys. Res. B **68**, 235 (1992).

[67] W. Hong, S. Hayakawa, Y. Gohshi, K. Maeda, S. Fukuda, M. Yanokura, K. Kimura, I. Tanihata, and M. Aratani, *Development of a high mass-resolution TOF-ERDA system for a wide mass range*, Nucl. Instr. and Meth. in Phys. Res. B **124**, 95 (1997).

[68] M. Döbeli, R. Ender, V. Liechtenstein, and D. Vetterli, *Time-of-light spectrometry applied to 2 MeV He RBS*, Nucl. Instr. and Meth. in Phys. Res. B **142**, 417 (1998).

[69] F. Busch, W.Pfeffer, B. Kohlmeyer, D. Schull, and F. Puhlhoffer, *A position-sensitive transmission time detector*, Nucl. Instr. and Meth. **171**, 71 (1980).

[70] J. Jokinen, J. Keinonen, P. Tikkanen, A. Kuronen, T. Ahlgren, and K. Nordlund, *Comparison of TOF-ERDA and nuclear resonance reaction techniques for range profile measurements of keV energy implants*, Nucl. Instr. and Meth. in Phys. Res. B **119**, 533 (1996).

[71] J. Jokinen, *Time-of-flight spectrometry of recoiled atoms in the analysis of thin films*, Acta Polytech. Scand. Appl. Phys. Series **212**, 1 (1997).

[72] J. Schader, B. Kolb, K. Sevier, and K. Groeneweld, *Electron ejection from beam-tilted-foil experiments*, Nucl. Instr. and Meth. **151**, 563 (1978).

[73] P. Koschar, K. Kroneberger, A. Clouvas, M. Burkhard, W. Meckbach, O. Heil, J. Kemmler, H. Rothard, K. Groeneveld, R. Schramm, and H.-D. Betz, *Secondary-electron yield as a probe of preequilibrium stopping power of heavy ions colliding with solids*, Phys. Rev. A **40**, 3632 (1989).

[74] V. Liechtenstein, T. M. Ivkova, E. Olshanski, A. Baranov, R. Repnow, R. Hellborg, R. Weller, and H. Wirth, *Preparation and evaluation of thin diamond-like carbon foils for heavy-ion tandem accelerators and time-of-flight spectrometers*, Nucl. Instr. and Meth. in Phys. Res. A **397**, 140 (1997).

[75] V. Liechtenstein, T. Ivkova, E. Olshanski, A. Baranov, R. Repnow, R. Hellborg, R. A. Weller, and H. L. Wirth, *Preparation and comparative testing of advanced diamond-like carbon foils for tandem accelerators and time-of-flight spectrometers*, Nucl. Instr. and Meth. in Phys. Res. A **438**, 79 (1999).

[76] E. Sternglass, *Theory of secondary electron emission by high-speed ions*, Phys. Rev. **108**, 1 (1957).

[77] R. Neugebauer, R. Wuensch, T. Jalowy, K. O. Groeneveld, H. Rothard, A. Clouvas, and C. Potiriadis, *Secondary electron emission near the electronic stopping power maximum*, Phys. Rev. B **59**, 11113 (1999).

[78] T. Conlon, *Materials characterization with MeV ions*, Nucl. Instr. and Meth. in Phys. Res. B **40–41**, 828 (1989).

[79] W. Lanford, H. Trautvetter, J. Ziegler, and J. Keller, *New precision technique for measuring the concentration versus depth of hydrogen in solids*, Appl. Phys. Lett. **28**, 566 (1976).

[80] P. Torri, J. Keinonen, and K. Nordlund, *A low-level detection system for hydrogen analysis with the reaction $^{1}H(^{1}5N, \alpha\gamma)^{12}C$*, Nucl. Instr. and Meth. in Phys. Res. B **84**, 105 (1994).

[81] J. Jokinen, P. Haussalo, J. Keinonen, M. Ritala, D. Riihelä, and M. Leskelä, *Analysis of AlN thin films by combining TOF-ERDA and NRB techniques*, Thin Solid Films **289**, 159 (1996).

[82] W. Bohne, J. Röhrich, and G. Röschert, *The Berlin time-of-flight ERDA setup*, Nucl. Instr. and Meth. in Phys. Res. B **136-138**, 633 (1998).

[83] M. Wielunski, M. Mayer, R. Behrisch, J. Roth, and B. Scherzer, *Simultaneous profiling of hydrogen and deuterium by 2.6 MeV ^{4}He ERDA using ΔE–E telescope detector*, Nucl. Instr. and Meth. in Phys. Res. B **122**, 113 (1997).

[84] S. Gujrathi and S. Bultena, *Depth profiling of hydrogen using the high efficiency ERD-TOF technique*, Nucl. Instr. and Meth. in Phys. Res. B **64**, 789 (1992).

[85] G. Boudreault, R. Elliman, R. Grötzschel, S. Gujrathi, C. Jeynes, W. Lennard, E. Rauhala, T. Sajavaara, H. Timmers, and T. Weijers, *Round Robin: Measurement of H implants in Silicon by ERD*, Poster at 15th Ion Beam Analysis -conference, Cairns, Australia (2001).

[86] M. Nieminen, S. Lehto, and L. Niinistö, *Atomic layer epitaxy growth of $LaGaO_3$ thin films*, J. Mat. Chem. **11**, 3148 (2001).

[87] B. Maurel and G. Amsel, *A new measurement of the 429 keV $^{15}N(p,\alpha\gamma)^{12}C$ resonance. Applications of the very narrow width found to ^{15}N and ^{1}H depth location. I. Resonance width measurement*, Nucl. Instr. and Meth. **218**, 159 (1983).

[88] G. Meyer and N. Amer, *Novel optical approach to atomic force microscopy*, Appl. Phys. Lett. **53**, 1045 (1988).

[89] A. Ott, J. Klaus, J. Johnson, and S. George, *Al_3O_3 thin film growth on Si(100) using binary reaction sequence chemistry*, Thin Solid Films **292**, 130 (1997).

[90] M. E. Bouanani, M. Hult, L. Persson, E. Swietlicki, M. Andersson, M. Östling, N. Lundberg, C. Zaring, D. Cohen, N. Dytlewski, P. Johnston, S. Walker, I. Bubb, and H. Whitlow, *Multivariate analysis method for energy calibration and improved mass assignment in recoil spectrometry*, Nucl. Instr. and Meth. in Phys. Res. B **94**, 530 (1994).

[91] Round Robin: Characterisation of the Thickness and Composition of Thin to Ultra-thin AlNO Films (IAEA coordinated project, coordinator N.P. Barradas).

[92] K. Oxorn, S. Gujrathi, S. Bultena, L. Cliche, and J. Minskin, *An iterative computer analysis package for elastic recoil detection*, Nucl. Instr. and Meth. in Phys. Res. B **45**, 166 (1990).

[93] N. P. Barradas, C. Jeynes, and R. Webb, *Simulated annealing analysis of Rutherford backscattering data*, Appl. Phys. Lett. **71**, 291 (1997).

[94] R. Fischer, M. Mayer, W. von der Linden, and V. Dose, *Enhancement of the energy resolution in ion-beam experimentswith the maximum-entropy method*, Phys. Rev. E **55**, 6667 (1997).

[95] E. Edelmann, K. Arstila, and J. Keinonen, to be published.

[96] E. Arai, H. Funaki, M. Katayama, and K. Shimizu, *Stoichiometry and profiling of surface layers by means of TOF-E ERDA and RBS*, Nucl. Instr. and Meth. in Phys. Res. B **68**, 202 (1992).

[97] P. Sigmund and K. Winterborn, *Small-angle multiple scattering of ions in the screened Coulomb region. I. Angular distributions*, Nucl. Instr. and Meth. **119**, 541 (1974).

[98] E. Szilagyi and F. Paszti, *Theoretical calculation of the depth resolution of IBA methods*, Nucl. Instr. and Meth. in Phys. Res. B **85**, 616 (1994).

[99] E. Szilágyi, L. Wielunski, and F. Pászti, *Theoretical approximation of energy distribution of elastically recoiled hydrogen atoms*, Nucl. Instr. and Meth. in Phys. Res. B **136–138**, 701 (1998).

[100] P. Bauer, E. Steinbauer, and J. Biersack, *The width of an RBS spectrum: influence of plural and multiple scattering*, Nucl. Instr. and Meth. in Phys. Res. B **64**, 711 (1992).

[101] P. Johnston, R. Franich, I. Bubb, M. Bouanani, D. Cohen, N. Dytlewksi, and R. Siegele, *The effects of large angle plural scattering on heavy ion elastic recoil detection analysis*, Nucl. Instr. and Meth. in Phys. Res. B **161–163**, 314 (2000).

[102] R. D. Franich, P. N. Johnston, I. F. Bubb, N. Dytlewski, and D. D. Cohen, *Efficiency enhancements to Monte Carlo simulation of heavy ion elastic recoil detection analysis spectra*, Nucl. Instr. and Meth. in Phys. Res. B **190**, 252 (2002).

[103] J. Slotte, A. Laakso, T. Ahlgren, E. Rauhala, R. Salonen, J. Räisänen, A. Simon, I. Uzonyi, Z. Kiss, and E. Somorjai, *Influence of surface topography on depth profiles obtained by Rutherford backscattering spectrometry*, J. Appl. Phys. **87**, 140 (2000).

[104] H. Metzner, M. Gossla, and T. Hahn, *Rutherford backscattering spectroscopy of rough films: Theoretical considerations*, Nucl. Instr. and Meth. in Phys. Res. B **124**, 567 (1996).

[105] R. Behrisch, S. Grigull, U. Kreissig, and R. Grötzschel, *Influence of surface roughness on measuring depth profiles and the total amount of implanted ions by RBS and ERDA*, Nucl. Instr. and Meth. in Phys. Res. B **136–138**, 628 (1998).

[106] H. Metzner, M. Gossla, T. Hahn, J. Conrad, and J.-H. Bremer, *Rutherford backscattering spectroscopy of rough films: Experimental aspects*, Nucl. Instr. and Meth. in Phys. Res. B **134**, 249 (1998).

[107] A. Kitamura, T. Tamai, A. Taniike, Y. Furuyama, T. Maeda, N. Ogiwara, and M. Saidoh, *Simulation of ERD spectra for a surface with a periodic roughness*, Nucl. Instr. and Meth. in Phys. Res. B **134**, 98 (1998).

[108] I.-M. Yesil, W. Assmann, H. Huber, and K. Löbner, *Simulation of surface roughness effects in ERDA*, Nucl. Instr. and Meth. in Phys. Res. B **136–138**, 623 (1998).

[109] S. Lindner, W. Bohne, A. Jäger-Waldau, M. Lux-Steiner, J. Röhrich, and G. Vogl, *Investigations of atomic diffusion at CIGSSe/ZnSe interfaces with heavy ion elastic recoil detection analysis (HI-ERDA)*, Thin Solid Films **403–404**, 432 (2002).

[110] J. R. Tesmer and M. Nastasi (ed.), *Handbook of Modern Ion Beam Materials Analysis* (Materials Research Society, Pittsburgh, USA, 1995).

[111] R. Behrisch, W. von der Linden, U. von Toussaint, and D. Grambole, *Surface layer destruction during ion beam analysis*, Nucl. Instr. and Meth. in Phys. Res. B **155**, 440 (1999).

[112] S. Walker, J. Davies, J. Forster, S. Wallace, and A. Kockelkoren, *Radiation damage during heavy ion elastic recoil detection analysis of insulating materials*, Nucl. Instr. and Meth. in Phys. Res. B **136-138**, 707 (1998).

[113] S. Wallace, A. Kockelkoren, M. Boudreau, P. Mascher, J. Forster, and J. Davies, *Hydrogen and Nitrogen Loss during ERD Analysis of Silicon (Oxy)nitrides*, Mat. Sci. Forum **248-249**, 381 (1997).

[114] H. Timmers, T. Weijers, R. Elliman, J. Uribasterra, H. J. Whitlow, and E.-L. Sarwe, *Threshold stoichiometry for beam induced nitrogen depletion of SiN*, Nucl. Instr. and Meth. in Phys. Res. B **190**, 428 (2002).

[115] R. Behrisch, M. Mayer, W. Jacob, W. Assmann, G. Dollinger, A. Bergmaier, U. Kreissig, M. Friedrich, G. Sun, D. Hildebrandt, M. Akbi, W. Schneider, D. Schleußner, W. Knapp, and C. Edelmann, *Quantitative analysis of deuterium in a-C:D layers, a Round Robin experiment*, J. Nucl. Mat. **281**, 42 (2000).

[116] R. Behrisch, V. Prozesky, H. Huber, and W. Assmann, *Hydrogen desorption induced by heavy-ions during surface layer analysis with ERDA*, Nucl. Instr. and Meth. in Phys. Res. B **118**, 262 (1996).

[117] G. Dollinger, M. Boulouednine, A. Bergmaier, T. Faestermann, and C. Frey, *Limits in elastic recoil detection analysis with heavy ions*, Nucl. Instr. and Meth. in Phys. Res. B **118**, 291 (1996).

[118] J. Likonen, S. Lehto, T. Sajavaara, J. Keinonen, and P. Coad, *Characterization of JET wall tiles with surface analytical techniques*, to be published.

[119] P. Johnston, I. Budd, S. Walker, W. Stannard, D. Jamieson, S. Dooley, D. Cohen, N. Dytlewski, and J. Martin, *Damage in semiconductor materials during heavy-ion elastic recoil detection analysis*, Nucl. Instr. and Meth. in Phys. Res. B **113**, 312 (1996).

[120] H. Huber, W. Assmann, S. A. Karamian, H. Mieskes, H. Nolte, E. Gazis, M. Kokkoris, S. Kossionides, R. Vlastou, R. Grötzschel, A. Mücklich, and W. Prusseit, *Heavy-ion induced damage of crystalline Ge and W in the 0.5–8 A MeV range*, Nucl. Instr. and Meth. in Phys. Res. B **146**, 309 (1998).

[121] M. Guina, N. Xiang, A. Vainionpaa, O. Okhotnikov, T. Sajavaara, and J. Keinonen, *Self-starting stretched-pulse fiber laser mode locked and stabilized with slow and fast semiconductor saturable absorbers*, Optics Lett. **26**, 1809 (2001).

[122] N. Xiang, M. Guina, A. Vainionpaa, J. Lyytikäinen, S. Suomalainen, M. Saarinen, O. Okhotnikov, T. Sajavaara, and J. Keinonen, *Broadband Semiconductor Saturable Absorber Mirrors in the 1.55-μm Wavelenght Range for Pulse Generation in Fiber*, J. Quantum Electronics **38**, 369 (2002).

[123] W. Weber, *Models and mechanisms of irradiation-induced amorphization in ceramics*, Nucl. Instr. and Meth. in Phys. Res. B **166-167**, 98 (2000).

[124] F. Baudenbacher, M. Bauer, H. Kinder, G. Dollinger, F. Ohnesorge, and W. Assman, *Impact and characterisation of heavy ion tracks on epitaxial growth*, Nucl. Instr. and Meth. in Phys. Res. B **107**, 327 (1996).

[125] S. Dhar, S. Gasiorek, M. Lang, K. Lieb, J. Keinonen, and T. Sajavaara, to be published.

[126] O. Espeso-Gil, T. Sajavaara, G. D. L. Paliza, G. García, F. Agulló-López, J. Cabrera, and A. Climent-Font, to be published.

[127] S. Gasiorek, S. Dhar, T. Sajavaara, K. Lieb, and J. Keinonen, to be published.

[128] T. Suntola, *Atomic layer epitaxy*, Thin Solid Films **216**, 84 (1992).

[129] M. Gustafsson, F. Roccaforte, W. Bolse, L. Ziegeler, and K. P. Lieb, *Oxygen-activated epitaxial recrystallization of Li-implanted* α*-*SiO_2, Phys. Rev. B **61**, 3327 (2000).